

Climate in a Bottle: Towards a Generative Foundation Model for the Kilometer-Scale Global Atmosphere

Noah D. Brenowitz Tao Ge Akshay Subramaniam Aayush Gupta
David M. Hall Morteza Mardani Arash Vahdat Karthik Kashinath
Michael S. Pritchard

NVIDIA, Santa Clara, CA, USA

Abstract

AI emulators offer a path to compressing, boosting limited ensembles, and improving the latency of interacting with petabyte-scale climate prediction data. However, prevailing auto-regressive paradigms offer limited flexibility, and are challenging to train on climate time horizons due to drifts, instabilities and component-coupling challenges. Conditionally generative models offer an appealing alternative. In this context we demonstrate a generative diffusion-based framework—Climate in a Bottle (*cBottle*)—for emulating global km-scale climate simulations and reanalysis on the equal-area HEALPix grid. *cBottle* consists of two model stages: a globally-trained coarse-resolution image generator that generates 100km (50k-pixel) fields given monthly average sea surface temperatures and solar conditioning, followed by a locally-trained 16x super-resolution stage that generates 5km (12.5M-pixel) fields; global super-resolution is made affordable using an overlapping patch-based multi-diffusion. Overall, *cBottle* shows promise as an emulator across a battery of climate model diagnostics, including diurnal-to-seasonal scale variability, large-scale modes of variability, tropical cyclone statistics, and trends of climate change and weather extremes. Moreover, *cBottle* is a step towards a foundation model, by bridging multiple data modalities (reanalysis and simulation) with corresponding utility beyond emulation to tasks such as zero-shot bias correction, climate downscaling, and channel in-filling. The code is available at <https://github.com/NVlabs/cBottle>.

1 Introduction

Knowing more, and planning better for the consequences of climate change are driving tremendous advances in the realms of climate simulation and Earth observation. With exascale computing and energy-efficient computational systems, petabytes of kilometer-scale climate data are being generated. Digital-twin efforts like the Destination Earth initiative [Bauer et al., 2021] and the Earth Virtualization Engines (EVE) project [Stevens et al., 2024] envision a world where high-fidelity global climate projections with local granularity are available to all with a degree of access and interactivity that provides a scientifically grounded basis for action. Further, digital twins aim to efficiently expose the data to new methods of analysis and proactive information production that will enable stakeholders to construct and interact with their own climate scenarios.

Easy access and low-latency interactivity, however, are nearly impossible with the current paradigm of petabyte-scale datasets generated and hosted by a handful of climate centers. Even if the access problem is unthrottled by moving data around, interacting with petabytes of data is virtually impossible. Generative artificial intelligence (AI) is poised to disrupt this paradigm by fully leveraging state-of-the-art architectures and algorithms optimized for performance on accelerated computing hardware.

For our purposes, we define a generative foundation model as a self-supervised climate simulator capable of producing realistic-looking samples that are climate-faithful measured by a set of diagnostics, and can be used to examine *what-if* scenarios not explicitly built into the model. Of course, climate science has long had such foundation models in the form of physics-based general circulation models. However, advances in AI are already fundamentally changing how weather and climate are simulated due to their ease of use, enhanced computational performance, and improved accuracy. Specifically, emulators of weather have proven to be skillful and orders-of-magnitude faster than traditional numerical simulation-based approaches to simulating

the weather across spatial and temporal scales [Pathak et al., 2022, Lam et al., 2023, Bi et al., 2023, Price et al., 2024, Bodnar et al., 2024]. Similarly, AI is proving to be efficient and faithful at emulating climate models and climate data, evaluated across a range of metrics on a wide variety of tasks [Watt-Meyer et al., 2024, Chapman et al., 2025, Cresswell-Clay et al., 2024, Watson-Parris et al., 2022]. A majority of these developments have resorted to the auto-regressive modeling paradigm, much like numerical weather and climate models that step forward in time evolving the state of the system modeled by governing systems of equations. Masked training and representation learning have also been proposed [Lessig et al., 2023].

Diffusion modeling [Ho et al., 2020, Song et al., 2020a, Karras et al., 2022] offers an alternative to the auto-regressive time-stepping approach by learning—and sampling—from a distribution of states. This is especially attractive for rapid analyses and informatics that do not require the full temporal evolution of the system. By the same token, they are not susceptible to instabilities or drifts (i.e., *hallucinations*) inherent to auto-regressive models, though admittedly many auto-regressive emulators perform surprisingly well for large numbers of steps [Watt-Meyer et al., 2024, Cresswell-Clay et al., 2024]. Further, diffusion models can be controlled by the user in a variety of ways, using *guidance* [Song et al., 2020a] to generate conditional distributions. Generative diffusion modeling has had tremendous impact across disciplines ranging from computer vision to science, and enjoys widespread adoption across the industry. Notably, it has been used in weather and climate for ensemble generation and uncertainty quantification [Li et al., 2024], probabilistic forecasting [Price et al., 2024], super-resolution (or downscaling) [Mardani et al., 2025], and data-assimilation [Rozet and Louppe, 2023, Manshausen et al., 2024].

A less explored yet promising direction is its application towards learning a compressed representation of massive climate datasets that generates, on demand, climate states steered by user-specified conditions and scenarios. Early examples included training deterministic emulators to predict the mean-state response of climate models to various forcings [Watson-Parris et al., 2022]. More recent efforts have extended this approach to stochastic emulators in the diffusion framework [Basseti et al., 2024, Quilcaille et al., 2022] as well as traditional dimensionality reduction approaches [Wang et al., 2025]. But these approaches have been limited to a small number of channels (typically surface temperature) at a coarse spatial resolution.

We develop a generative diffusion-based framework that we call “Climate in a bottle” (*cBottle*) to emulate multimodal climate data. *cBottle* uses a cascaded approach [Ho et al., 2021] to generating km-scale samples: a coarse-resolution generator conditioned on user-specified inputs (time of day, time of year, and monthly-averaged sea surface temperature (SST)) and a 16x super-resolution module. Both steps use generative diffusion models, and either can be used independently, enabling generation of coarse-resolution samples and/or super-resolution to km-scale.

cBottle has a few key properties:

1. Multi-modality and domain transfer: Bridges ERA5 and ICON km-scale datasets, enables generation of km-scale climate states that exploits the information content contained across ERA5 and ICON
2. Versatility across a few useful tasks: Bias-correction, channel in-filling, downscaling
3. Climate faithfulness: Generates realistic climatology, climate variability across timescales, large-scale modes, and extreme weather statistics
4. Data efficiency: Can be trained on as little as 4 weeks of simulation output
5. Extreme compression: Encapsulates km-scale climate model and reanalysis outputs into a few GB of neural network weights, and offers 256x compression ratio per channel
6. Speed and scale: Low-latency generation of km-scale samples and scalability to higher resolutions and more modalities

These properties of *cBottle* offer potential pathways towards: (i) solving the data and informatics challenges of km-scale climate data; and (ii) building a generative foundation model for an interactive digital twin.

2 Methods

2.1 Overview

In this section we describe the components of our diffusion-based generative climate model shown in Figure 2. The architecture and diffusions are formulated on the sphere using the increasing popular HEALPix grid

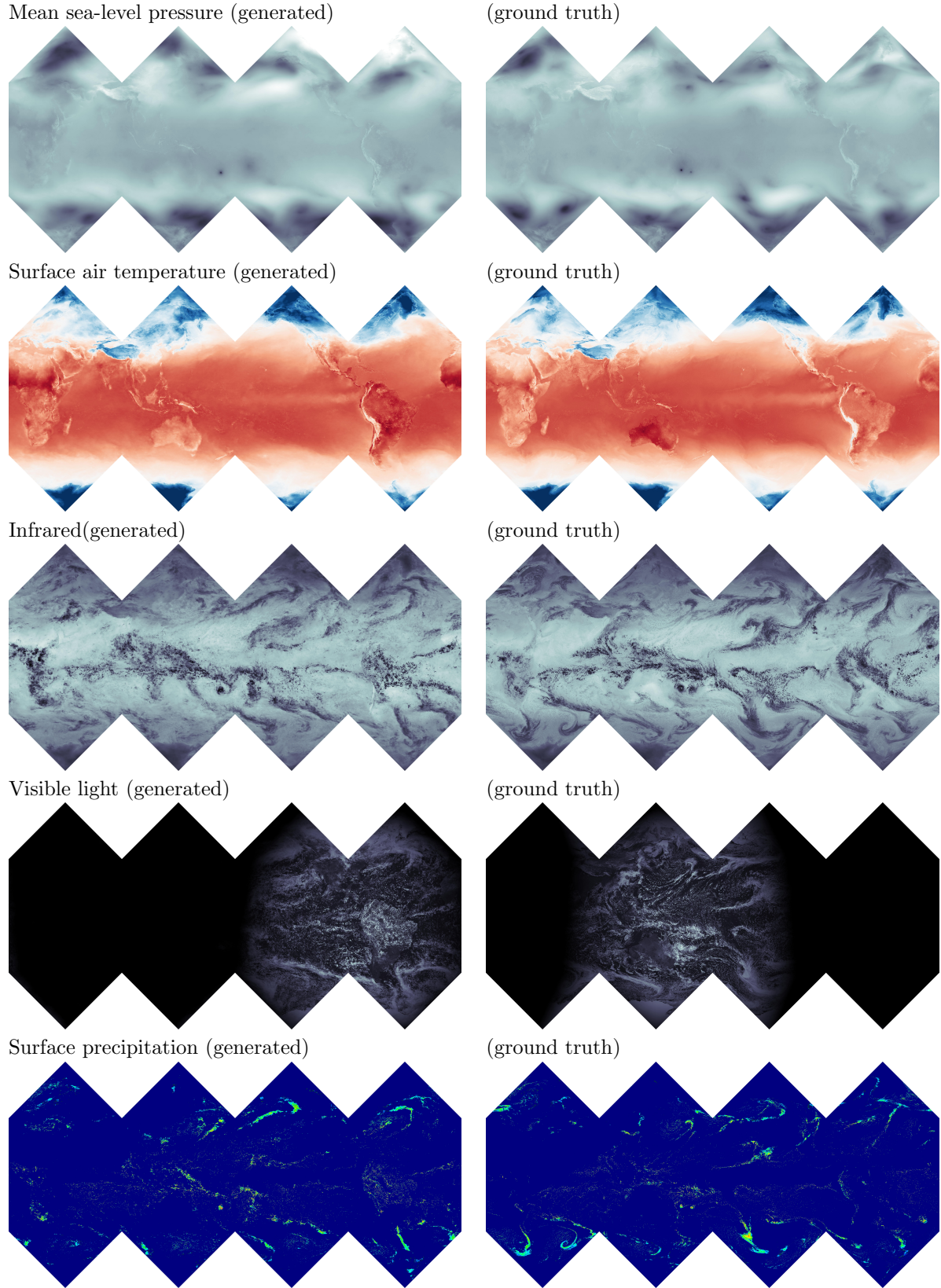


Figure 1: High resolution (HPX1024) samples from the ICON data (right) and synthesized by cBottle given sea surface temperature and time conditionings (left). Note these are not identically paired. For each field the same colormap is used, but to highlight the visual similarity we do not include color-bars. More quantitative comparisons will follow.

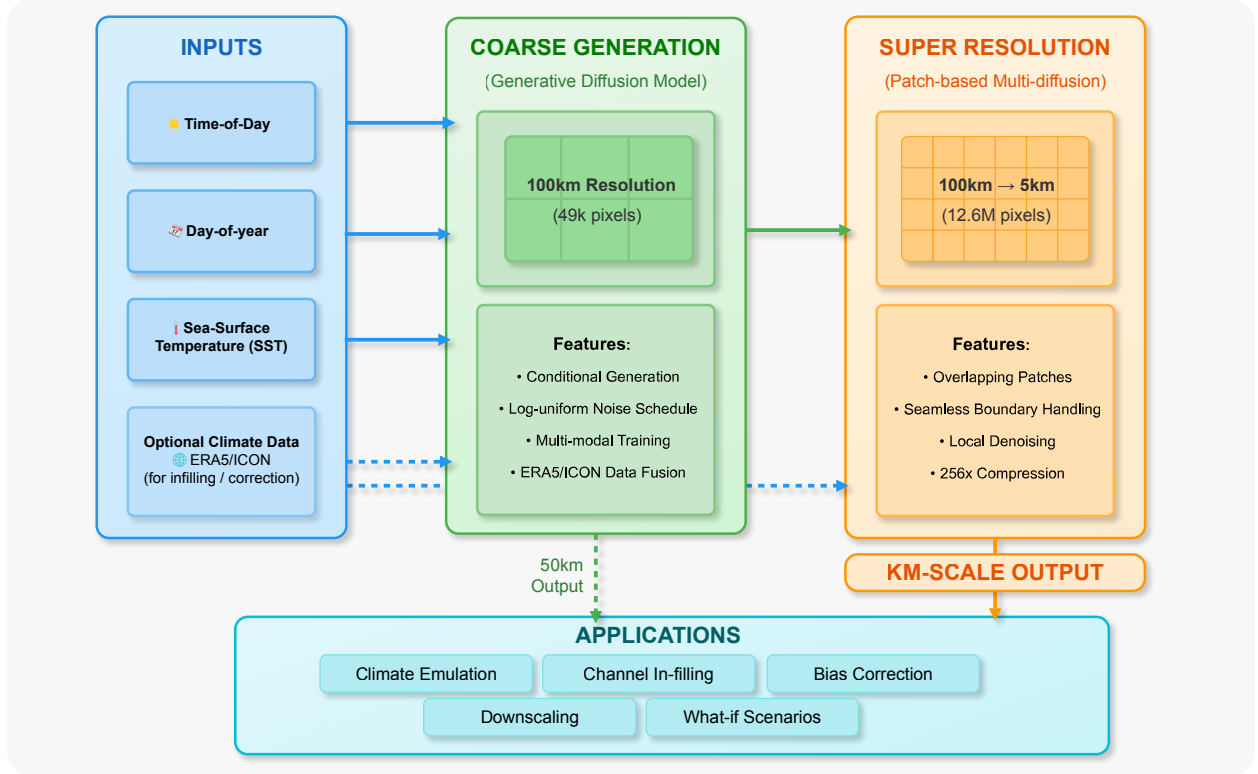


Figure 2: Climate in a Bottle (cBottle) Model Architecture. A cascaded approach with two complementary diffusion models that produces kilometer-scale climate data on demand. Inputs (left) include time-of-day, date-of-year, and SST, which feed into the Coarse Generation model (center) to produce 100km resolution outputs. These are then processed by the Super Resolution model (right) to transform coarse outputs to 5km resolution. This architecture enables climate emulation, channel in-filling, bias correction, downscaling, and what-if scenario exploration.

(Section 2.2). We train on two dense global datasets (Section 2.3) using a masked training strategy (Section 2.6). We introduce the preliminary details of diffusion modeling (Section 2.4) and our strategy for scaling to high-resolution data (Section 2.5). Finally, we present the architectures and hyper-parameters used for training our coarse image and video models, and the super-resolution model (Section 2.7).

2.2 HEALPix and Padding

Using AI for global data poses a geometric challenge of appropriately representing data on a spherical surface. To this end, HEALPix [Gorski et al., 2005] grids offer an attractive solution with an equal area grid structure that also has iso-latitude properties and a hierarchical indexing scheme for multi-resolution workflows. The HEALPix grid is constructed of 12 faces with each face containing a square $2^l \times 2^l$ grid of pixels where l represents the resolution level of the grid. This structure makes it very friendly for deep-learning algorithms, especially for convolutional architectures and has been used in [Krachmalnicoff and Tomasi, 2019], [Perraudin et al., 2019] and [Karlbauer et al., 2024]. The equal area property is also particularly desirable for diffusion training. Due to these desirable properties, we use the HEALPix grid as the spherical discretization method in this work. A common convention for HEALPix grids refers to the length of each face $N_{side} = 2^l$. We refer to two main global grids: HPX64 ($N_{side} = 64$) corresponding to 100km resolution (49152 pixels) and HPX1024 ($N_{side} = 1024$) at 6km resolution (12,582,912 pixels).

2.2.1 Global modeling

For coarse resolution applications (below HEALPix level 8), we use architectures similar to [Mardani et al., 2025] that were designed for 2D rectangular domains. This is done by adapting the convolution operations in the architecture to perform convolutions on each HEALPix face independently. However, boundaries between HEALPix faces are not handled by such an approach and can cause artifacts. To address this, we pad each face using the protocol outlined in [Karlbauer et al., 2024] by the number of pixels needed for the convolution operation instead of relying on any implicit padding methods supported by convolution operations.

Consider a field represented on a level l the HEALPix grid, $x \in \mathbb{R}^{c_{in} \times 12 \times 2^l \times 2^l}$. One may apply a discrete convolution kernel $\mathcal{K}_{conv} \in \mathbb{R}^{c_{out} \times c_{in} \times 2k+1 \times 2k+1}$ as follows:

$$x = (x_1, x_2, \dots, x_{12}), \quad x_f \in \mathbb{R}^{c_{in} \times 2^l \times 2^l} \quad (1)$$

$$x^p = \mathcal{P}(x; k) = (x_1^p, x_2^p, \dots, x_{12}^p), \quad x_f^p \in \mathbb{R}^{c_{in} \times (2^l+2k) \times (2^l+2k)} \quad (2)$$

$$y_f = \mathcal{K}_{conv} * x_f^p, \quad y_f \in \mathbb{R}^{c_{out} \times 2^l \times 2^l} \quad (3)$$

$$y = (y_1, y_2, \dots, y_{12}), \quad y \in \mathbb{R}^{c_{out} \times 12 \times 2^l \times 2^l} \quad (4)$$

where x_f and y_f are the pixels of x and y respectively on the HEALPix face f , $\mathcal{P}(\cdot; k)$ is the padding operation of [Karlbauer et al., 2024] and $*$ indicates the convolution operation. Figure SI3 shows a schematic of how the UNet architecture of [Song et al., 2021] is adapted to work on global HEALPix fields.

2.2.2 Local modeling

Modeling of high resolution fields, like kilometer-scale climate model outputs, is prohibitively expensive using global approaches. To make this tractable, we use the multi-diffusion approach outlined in Section 2.5 and adapt that to spherical manifolds using the HEALPix grid and HEALPix padding. We define a new spatial sampling operator $\mathcal{G}_i : \mathcal{X} \rightarrow \mathcal{X}_{local,i}$ as a composition of the padding operator $\mathcal{P}(\cdot; N/2)$ and the 2D sampling operator \mathcal{F}_i defined in Section 2.5. Here N represents the patch size used in the multi-diffusion approach. The global denoiser can then be represented as

$$\mathcal{D}_\theta(\mathbf{x}_t) = \frac{\sum_i \mathcal{G}_i^{-1}(\Phi_\theta(\mathcal{G}_i(\mathbf{x}_t) | \mathcal{G}_i(y), \sigma))}{\sum_i \mathcal{G}_i^{-1}(J_N)} \quad (5)$$

$$\mathcal{G}_i(\mathbf{x}_t) = \mathcal{F}_i(\mathcal{P}(\mathbf{x}_t; N/2)), \quad (6)$$

Figure 3 shows a schematic of this approach.

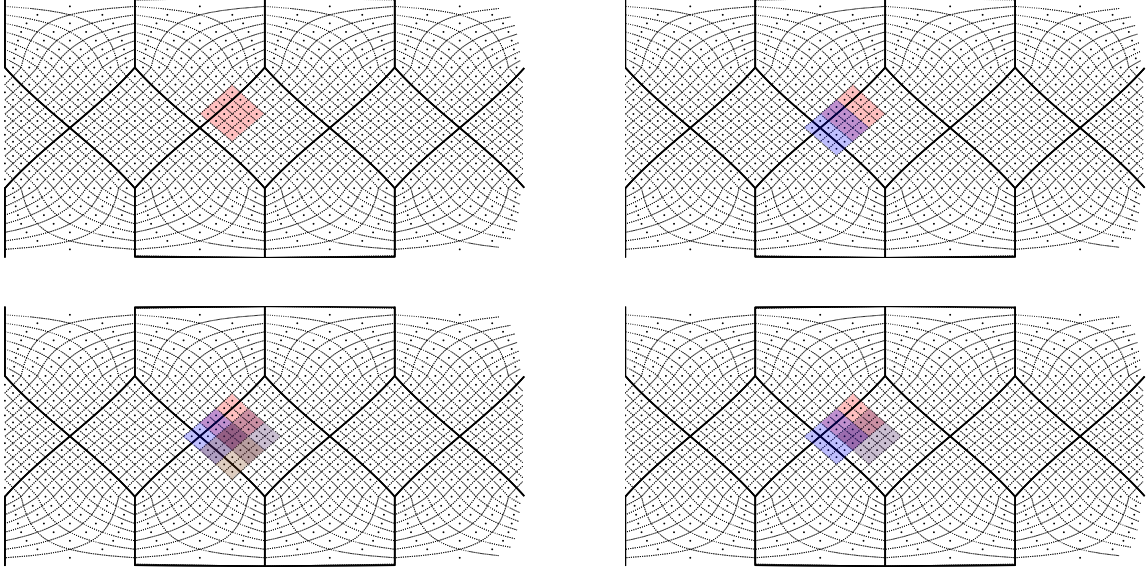


Figure 3: Schematic showing the multi-diffusion approach for spherical geometry with HEALPix grids. A sequence of the overlapping patch sampling protocol is shown going clockwise from the top left. Each colored region indicates a single patch and overlap between the patches minimizes boundary artifacts by combining patch representations into a global representation following 14.

2.3 Datasets

The inputs and outputs we trained with are displayed in Tab. 1. Briefly, the models are trained to generate 3D states of the atmosphere and some key 2D variables relevant to climate impacts (precipitation, surface air temperature, downwelling short-wave) and observations (top of atmosphere radiative fluxes).

Our models are trained on two global datasets: the ECMWF Reanalysis version 5 (ERA5)[Hersbach et al., 2020] which is observationally constrained, and a global storm resolving simulation with the ICON climate model [Hohenegger et al., 2023], which is a free-running simulation unpaired with reality.

ERA5 ERA5 is a commonly used dataset that represent the best guess of the global atmospheric state at a coarse resolution of 25 km. Briefly, it is created by running a data assimilation algorithm that incorporates observations into ECMWF’s numerical model. However, it is not available at a high enough resolution in space or time to resolve meso-scale motions on kilometer scale, and in particular deep convection. The ICON simulation fills in this gap since it is available at a global 5km resolution, but is not paired with reality. For pre-processing, we retrieved hourly ERA5 data for 1980–2018 (inclusive) via the data lake at the National Energy Research Computing Center (NERSC) at 0.25° resolution on the lat-lon grid. The 3d atmospheric states are available on pressure levels. We then regridded this using bilinear interpolation to the HEALPix grid with $N_{side} = 256$. For training the coarse-resolution model, this coarsened by averaging pooling to an $N_{side} = 64$. We train on years 1980–2017 (inclusive) and validate on 2018, though many of our climate diagnostics below are also computed on the validation set (as is common in generative modeling).

ICON Cycle 3 The ICON data is a free-running simulation with the ICON atmospheric model coupled to a dynamic ocean and land. The atmospheric component solves the nonhydrostatic fluid mechanics equations on a global ico-sahedral mesh with a resolution of around 5 km. Unlike ERA5 the model explicitly resolves certain convective motions so a convection parameterization is not used. So even beyond the simple increase in resolution, we expect this to increase the fidelity of the precipitation and cloud fields in this dataset relative to ERA5 where these processes are parameterized. Furthermore, because the ocean and land are dynamically coupled to the atmosphere, we expect this run to obey conservation of heat, momentum and moisture between

Targets	Shape	Datasets used for	2D	3D
Single level fields				
liquid water path	X	icon+era	✓	✓
ice water path	X	icon+era	✓	✓
2m air temperature	X	icon+era	✓	✓
surface zonal wind	X	icon+era	✓	✓
surface meridional wind	X	icon+era	✓	✓
Outgoing long wave radiation	X	icon	✓	✓
Outgoing shortwave radiation	X	icon	✓	✓
mean sea level pressure	X	icon+era	✓	✓
precipitation (total)	X	icon+era	✓	✓
downwelling SW at surface	X	icon	✓	✓
sea surface temperature (snapshot)	X	icon+era	✓	✓
sea ice concentration	X	icon+era	✓	✓
Pressure level variables @ [1000, 850, 700, 500, 300, 200, 50, 10] mb				
U	P, X	icon+era	✗	✓
V	P, X	icon+era	✗	✓
T	P, X	icon+era	✗	✓
Z	P, X	icon+era	✗	✓
Inputs				
Monthly mean SST	X	era5 = AMIP Monthly SST icon = rolling mean	✓	✓
Day of year			✓	✓
Hour of day			✓	✓
Label			✓	✓

Table 1: Input and target variables with dataset sources and dimensionality. X = space, P = levels.

these different components, unlike in the ERA5 where the observations (rather than conservations) are king.

We obtained O(PB) of ICON data (ngc3028) of the nextGEMS cycle 3 simulations [Koldunov et al., 2023] in zarr format from DKRZ’s JupyterHub server. This dataset was stored on the HEALPix grid with $N_{side} = 1024$, corresponding roughly to a resolution of $\sqrt{A/(12N_{side}^2)} = 6.3\text{km}$. Prior to our handling of the data it was interpolated using nearest neighbors from the native icosahedral grid. Five years of this data are available at 3-hour (3D) and 30-minute (2D) resolution in time. Conveniently, this dataset featured pre-coarsened data (again using averaging pooling) at our coarse-resolution of $N_{side} = 64$. We interpolated this coarse data to fixed pressure levels using linear interpolation in the vertical direction. To fill in values at pressure level locations that are below the surface, we use extrapolation based on hydrostatic balance constraints and an assumption of a constant temperature lapse rate of 6.5 K/km for temperature and geopotential. For all other variables, we use constant extrapolation down from the surface. This procedure approximately reproduces ERA5’s undocumented procedure for filling-in below-surface levels. We train on 2020-01-20 03:00:00 through 2024-03-06 12:00:00 (inclusive) and validate on 2024-03-06 15:00:00 through 2025-07-22 00:00:00.

AMIP SST Forcing Our models take a monthly time-scale SST as an input. For the ERA5 data which is paired with reality, we linearly interpolate the adjusted monthly SST time series following the AMIP protocol [Gates et al., 1999]. Specifically we downloaded the file: input4MIPs.CMIP6Plus.CMIP.PCMDI.PCMDI-

AMIP-1-1-9.ocean.mon.tosbcs.gn from the Earth System Grid Federation, and use bilinear interpolation to map it to HPX64 resolution. For the ICON data on the other hand, we compute a rolling window average in time with a window size of 30 days based on the HPX64 spatial and daily temporal resolution data in the ICON dataset.

2.4 Diffusion models

Background Let $p_{\text{data}}(\mathbf{x})$ denote the data distribution with standard deviation σ_{data} . We define the diffusion process as a pair of Markov chains over the states $\{\mathbf{x}_0, \mathbf{x}_1, \dots, \mathbf{x}_T\}$. The forward process gradually corrupts the data by adding i.i.d. Gaussian noise with standard deviation σ , eventually transforming the data into pure noise. Specifically, the final state satisfies $\mathbf{x}_T \sim \mathcal{N}(0, \sigma_{\text{max}})$, where $\sigma_{\text{max}} \gg \sigma_{\text{data}}$. The reverse process then attempts to denoise samples from this noisy distribution, ideally recovering samples from the original data distribution, i.e., transforming $\mathbf{x}_T \sim \mathcal{N}(0, \sigma_{\text{max}})$ back into $\mathbf{x}_0 \sim p_{\text{data}}(\mathbf{x})$.

In this work, we adopt the score-based diffusion framework [Song et al., 2021, Mardani et al., 2025], which learns this denoising process via a score-matching network. The training objective is given by

$$\arg \min_{\theta} \mathbb{E}_{\mathbf{x} \sim p_{\text{data}}} \mathbb{E}_{\sigma \sim p_{\sigma}} \mathbb{E}_{\epsilon \sim \mathcal{N}(0, \sigma^2 \mathbf{I})} \|\mathcal{D}_{\theta}(\mathbf{x} + \epsilon; \sigma) - \mathbf{x}\|^2, \quad (7)$$

where the learned denoiser $\mathcal{D}_{\theta}(\cdot; \sigma)$ approximates the score function according to $\nabla_{\mathbf{x}} \log p(\mathbf{x}; \sigma) \approx \frac{\mathcal{D}_{\theta}(\mathbf{x}; \sigma) - \mathbf{x}}{\sigma^2}$. Here, p_{σ} denotes the noise level distribution used during training.

To sample from the model, we employ the Elucidated Diffusion Model (EDM) sampler proposed by [Karras et al., 2022], which solves the corresponding reverse-time ordinary differential equation (ODE):

$$f d\mathbf{x} = -\dot{\sigma}(t)\sigma(t)\nabla_{\mathbf{x}} \log p(\mathbf{x}; \sigma(t)) \quad (8)$$

where $\dot{\sigma}(t)$ is the time derivative of the noise schedule $\sigma(t)$.

Specifically, we use Algorithm 2 from Karras et al. [2022], with the S_{churn} parameter set to 0.

Diffusions on the sphere To train diffusion models on the sphere, the noise $\epsilon_i \sim \mathcal{N}(0, 1)$ is drawn independently for every pixel $1 \leq i \leq 12 \cdot 4^l$. Because the HEALPix pixels are all equal area, we conjecture that this is identical to the pixel-wise average of a finite-variance continuous Gaussian process on the sphere.

Tuning noise schedules for non-stationary signals The choice of noise schedule during training (p_{σ}) and inference is crucial for the quality of diffusion model. We find that settings commonly used for image generation [Karras et al., 2022] do not work well across the dozens of atmospheric observables, each with different spectral characteristics. Moreover, compared to image datasets, these data are highly non-stationary in space and time. Climatology explains much of the variance of the atmosphere, but the mean of all cat images does not look like a cat. In particular, we find that our models cannot produce the seasonal or diurnal cycles using the settings from Karras et al. [2022] (see Sec 3.2.4).

The basic issue is known as the *signal leak bias* when a model is not trained with enough noise to swamp the signal [Everaert et al., 2023]. As a rough criterion, the noise levels sampled during training should be large enough to completely mask/unmask the signal when represented in *any basis*—not just the canonical basis in pixel space. Intuitively, if we fail to add enough noise then large-variance signals like season or hour of day can be detected simply by filtering the data enough. More concretely, the smallest σ_{min} should be chosen so that

$$v'(x + \sigma_{\text{min}}\epsilon) \approx v'x \quad (9)$$

and the largest so that

$$v'(x + \sigma_{\text{max}}\epsilon) \approx \sigma_{\text{max}}v'\epsilon \quad (10)$$

for any vector $\|v\| = 1$.

Criteria for $\sigma_{\{\text{min}, \text{max}\}}$ can be derived by starting from the observation that $E|v'\epsilon|^2 = |v|^2 = 1$, so that (9) and (10) are satisfied by choosing

$$\sigma_{\text{min}}^2 \lesssim \inf_{\|v\|=1} E|v'x|^2 \quad (11)$$

$$\sigma_{\text{max}}^2 \gtrsim \sup_{\|v\|=1} E|v'x|^2. \quad (12)$$

The *signal leak bias* occurs when σ_{max}^2 is too small. When σ_{min} is too large, the diffusion model will not denoise the lower-amplitude modes of the data.

Note that (12) is equal to the variance explained by the maximum principal component of the data. Recall that the overall variance can be decomposed $n = \text{TrCov}(x) = \sum_i s_i^2$ where n is the dimension of x (pixels and channels). To understand the behavior for changing n it is useful to discuss the fraction of variance explained by a singular value $\tilde{s}_i^2 = s_i^2/n$, and expect this fraction to converge as we refine the resolution. This implies then, that $\sigma_{max}^2 \gtrsim n\tilde{s}_1^2 = O(\sqrt{n})$.

In atmospheric science, the seasonal cycle and diurnal cycles are the dominant modes of variability since they are: 1) planetary in spatial scale; and 2) large in amplitude. In mid-latitude land locations, the daily high and low temperature are separated by $\sim 5 - 10^\circ\text{C}$, while the seasonal cycle is $\sim 10 - 20^\circ\text{C}$. Other variables don't have as strong a seasonal cycle over as large an area so we take the conservative estimate that the seasonal cycle explains 5% of the global variance across our whole variable set. The HPX64 model has about 30 channels in total and 49152 pixels. So this would imply a $\sigma_{max}^2 \gtrsim 300$. This is far larger than the range of the hyper parameters used for this resolution in typical image generation [Karras et al., 2022]. Similar analysis can explain the observation that generating higher-resolution images requires larger noise levels [Chen, 2023].

To estimate σ_{min} one could also use principal component analysis in theory, but in practice this is difficult. In practice, power spectral analysis works well for identifying high frequency modes. We also often choose σ_{min} based on the precision required for practical applications. Choosing σ_{min} too large manifests as an incorrectly flat spectra for the highest wave numbers (see e.g., the Z500 power spectra presented by Price et al. [2024]).

While one can tune the log-normal distribution to fully cover the dynamic range of the data $[\sigma_{min}, \sigma_{max}]$, we have found that sample quality is sensitive to shifts in the mean of the log-normal distribution. As a simpler approach, we propose a log-uniform noise schedule

$$p_\sigma \propto \sigma^{-1}, \sigma_{min} \leq \sigma \leq \sigma_{max}. \quad (13)$$

Because this is uniform in $\log \sigma$ we call it a "log-uniform" noise distribution. In earlier tests on the 2D data alone without SST conditioning, we achieved similar results with the power law distribution used by Price et al. [2024]. In practice, we set $\sigma_{min} = 0.02$ and $\sigma_{max} = 200$, settings which span the dynamic range of several of our variables (see Figure SI12). Although in hindsight we should have decreased it further for the smoothest fields like Z500. For inference, we use the same sampler as Karras et al. [2022] but with these settings.

2.5 Multi-diffusion

Emulating ICON at HPX1024 resolution poses substantial computational challenges due to the massive size of this km-scale global dataset. Directly applying a traditional diffusion model to the full-resolution domain is infeasible as it would require over 2,000 GB of GPU memory, assuming a linear relationship between spatial resolution and memory footprint. This far exceeds the capacity of current hardware, even on high-end multi-GPU systems.

To address the computational bottleneck and take advantage of the inherently local nature of super-resolution tasks, multi-diffusion [Bar-Tal et al., 2023] is adapted as a scalable and memory-efficient sampling strategy. It enables high-resolution generation without sacrificing global spatial coherence or requiring model architecture changes.

The central idea behind multi-diffusion is to replace the global denoiser used in standard sampling algorithms with an aggregated local denoiser. At each sampling step, the aggregated local denoiser operates on the global feature map in a sliding-window fashion, denoising it patch by patch. These locally denoised patches are then reassembled to reconstruct the global feature map. This procedure is illustrated in Figure SI5.

Given a pretrained local denoiser Φ_θ and a set of spatial sampling operators $\mathcal{F}_i : \mathcal{X} \rightarrow \mathcal{X}_{\text{local},i}$, the global denoiser can be represented as an aggregation of local denoisers:

$$\mathcal{D}_\theta(\mathbf{x}_t) = \frac{\sum_i \mathcal{F}_i^{-1}(\Phi_\theta(\mathcal{F}_i(\mathbf{x}_t) | \mathcal{F}_i(y), \sigma))}{\sum_i \mathcal{F}_i^{-1}(J_N)}, \quad (14)$$

where $\mathcal{F}_i^{-1} : \mathcal{X}_{\text{local},i} \rightarrow \mathcal{X}$ denotes the inverse operation that maps local patches back to the global space, $y \in \mathcal{Y}$ denote the spatial conditions, $\mathcal{X}_{\text{local}} = \mathbb{R}^{C_{\text{out}} \times N \times N}$ denotes the local target space, $\mathcal{Y} = \mathbb{R}^{C_{\text{in}} \times N \times N}$ denotes the local condition space, N is the patch size, and $J \in \mathcal{X}_{\text{local}}$ is an all-one matrix of size $N \times N$ used to account for the number of overlapping patches at each location in the global map.

A fundamental design principle of multi-diffusion is the global sharing of the latent representation X across all local patches. The spatial sampling operators \mathcal{F}_i define the patch layout, including the extent of overlap between adjacent regions and the total number of patches required to span the full domain. Introducing overlap is essential for reducing boundary artifacts and promoting consistency across patches. However, increasing the overlap also raises the computational cost, as it leads to a larger number of denoiser evaluations during sampling. As demonstrated in the ablation study in Subsection 3.2.4, strong performance can be maintained even with minimal overlap, enabling a favorable trade-off between quality and efficiency.

2.6 Multi-modal masking

Since we intend our framework to extend to a variety of data sources, with different coverage in space, time, and the included fields, we have designed the model to handle masked training. For example, we learned that the ERA5 shortwave and longwave radiation fields are corrupted by a known, but undocumented, bug which appears as clear stripe-like artifacts that point North-West (see Fig 17). This is caused by a random seed in the radiation scheme being set to *lat + lon* in every atmospheric column [Chantry, 2024]. Therefore, as noted in Tab. 1, we do not use the fields from ERA5 for training our models, and instead rely on the multi-modal diffusion modeling to fill in this gap.

Our approach is to simply train a diffusion model to generate the union of all channels present in all the datasets, but have modified the code to support masking. This approach may seem inflexible compared to flexible architectures [Bodnar et al., 2024] but it is reasonable to scale since it has long been known how to represent the state of the atmosphere using dense grids of the known state variables.

Specifically, during training, any masked values in the noisy image $x + n$ and target x are filled with 0 before calling the network and computing the loss. We then normalize the loss by the fraction of masked out data points, so that the training equally weights modalities with different numbers of observables. Psuedo-code for this approach is shown in SI E.

2.7 Architectures and hyperparameter settings

We mostly reuse the standard UNet architecture used in diffusion modeling (the so-called Song-UNet in Karras et al. [2022], Mardani et al. [2025] and others). However, it was necessary to add position and temporal embedding (Figure SI2) to allow the diffusion model to learn non-stationary signals in space and time, and temporal attention layers to support video diffusion. Table 2 summarizes our three model variants.

Calendar Embedding Producing an accurate seasonal and diurnal cycle required a calendar and hour embedding strategy. We take care to use an embedding that respects the periodicity of these inputs. This is given by

$$f_{4k} = \cos\left(2\pi k \frac{\text{doy}}{365.25}\right) \quad (15)$$

$$f_{4k+1} = \sin\left(2\pi k \frac{\text{doy}}{365.25}\right) \quad (16)$$

$$f_{4k+2} = \cos(kt) \quad (17)$$

$$f_{4k+3} = \sin(kt). \quad (18)$$

Here, the day of year (doy) is a scalar representing the time since the beginning of the year, and the time of day (t) is the local solar time in units radians $t = 2\pi(\frac{\text{second of day}}{86400} + \frac{\text{lon}}{360})^1$. In the architectures below we use $k = 1, \dots, 8$, and concatenate these inputs along with other image-like conditioning (e.g., monthly-averaged SST) and noisy target image.

¹Due to an implementation error we actually used *second - lon*.

	cBottle-3d	cBottle-video	cBottle-SR
Number of parameters	149M	282M	330M
Target channels	3D	3D	2D
Architecture	Song UNet	Song UNet	Song UNet
Learned Position Encoding	✓	✓	✓
Calendar embedding	✓	✓	✗
Trained on	ICON+ERA5	ICON+ERA5	ICON
Grid	HPX64 (49152)	HPX64 (49152)	128x128 crops of HPX1024
Training domain	global	global	crops
Total examples trained	9,856,000	2,160,000	95,520 samples / 191M patches
Batch size	64 (3M images) 256 (3-10M)	32	960
Optimizer	Adam	Adam	SGD
Learning rate	0.0001	0.0001	0.0001
Noise distribution (p_σ)	log-uniform 0.02–200	log-uniform 0.02–1000	log-normal $P_{\text{mean}} = -1.2$ $P_{\text{std}} = 1.2$
Computational Profile			
Hardware trained on	16xH100	32xH100	64xH100
Examples/GPU-second (train)	6.7	0.32	35.4 patches

Table 2: Comparison of *cBottle* model variants.. A training example is defined a single HPX64 image for the the coarse models but is a single 128x128 crop for cBottle-superres.

Learned position embedding To allow the diffusion model to learn non-stationary spatial structures like climatology, we add a learned position embedding. After the initial convolution embedding of the image-like inputs (calendar, noisy image and monthly-averaged SST), a learned positional embedding for each pixel $49152 \times c$ is added. The position embedding is initialized with independent standard normal random numbers.

2.7.1 Video Generation Extension

Let $x \in \mathbb{R}^{T \times C \times X}$ denote an atmospheric trajectory of T evenly spaced frames with X pixels each. While the coarse image *cBottle* produces realistic atmospheric snapshots, T successive samples in time produce a sequence that lacks temporal coherence due to the independence of each sample.

Temporal Attention We extend *cBottle* to video generation by augmenting the 2D UNet architecture with temporal self-attention layers, following factorized space-time approaches [Ho et al., 2022, Blattmann et al., 2023]. The architecture preserves the UNet backbone of *cBottle*, but introduces temporal layers at the end of spatial blocks. Within each UNet block, we first apply spatial modules with the time dimension folded into the batch dimension. For blocks with temporal attention, we fold the spatial dimension into the batch dimension, and then apply bidirectional self-attention across frames per pixel, using the channels as the embedding dimension. A learned relative-time embedding $R_{\Delta t} \in \mathbb{R}^{2T-1}$ capturing frame-to-frame dependencies based on temporal distance Δt is added to the pre-softmax logits. The temporal attention output is then residually added to the main branch.

Masked-Conditioning To enable flexible inference capabilities, we adopt a masked-conditioning training scheme inspired by MCVD [Voleti et al., 2022]. During training, we randomly sample mask patterns $m \in \{0, 1\}^T$ (where 1 indicates observed frames) from a categorical distribution p_{mask} that blends several tasks:

Bernoulli random frame dropout, masking all but the first or last few frames contiguously, masking middle frames while keeping endpoints visible, and full sequence masking. On top of the calendar embedding and monthly-mean SST conditioning that the image-model uses, we add this masked sequence (ground truth at unmasked positions and zeros at masked positions) and the binary mask indicator as conditioning concatenated channel-wise with the input. The video diffusion training objective is identical to the image diffusion objective, but with this additional per-sample masked-conditioning and the loss averaged across the T frames.

2.7.2 Model Settings

cBottle-3D The coarse image model generates HPX64 fields. The coarse resolution image generator uses the standard settings for the Song-UNet presented by Karras et al. [2022], but we found the 3D training was made more stable by increasing base model embedding dimension from 128 to 192. The source dataset is identified with a label (ERA5 or ICON) which is randomly dropped for 1/4 samples to encourage the model to learn features across both datasets. This label is provided to the UNet in the same manner as the imagenet class label in Karras et al. [2022]. Self-attention is only used on the coarsest resolution stage (8x8). All convolutional layers are implemented on the HPX grid using the padding approach described in Section 2.2.1. 32 channels are devoted to calendar embedding. The model was trained from scratch on a 50-50 mix of ICON and ERA5 data on 32 H100 GPUs. Even (odd) ranks were trained with ERA5 (ICON). The model was trained to 3 million samples (with repeats) with a batch size of 64 (~ 50000 steps) when the log probability loss started to plateau, and then the batch size was increased to 256 until 10 million samples. The Adam optimizer [Kingma and Ba, 2014] was used with a learning rate of 10^{-4} . During training the model uses the log-uniform noise distribution (p_σ) with $\sigma_{min} = 0.02$ and $\sigma_{max} = 200$. For inference, we use the power law sampler proposed by Karras et al. [2022] with these same settings.

This unified training approach enables the video model to perform multiple tasks at inference time: generate entire sequences unconditionally, predict future frames given initial states, or infill arbitrary temporal gaps.

cBottle-video The video model generates 3-day sequences with 6-hour resolution ($T = 12$ frames) at the same HPX64 resolution of the image-based *cBottle*. Because T correlated frames carry more redundant signal, we keep the same log-uniform noise schedule (with $\sigma_{min} = 0.02$) and increase σ_{max} from 200 to 1000 in both training and inference to preempt *signal leak bias* (see Subsection 2.4). We insert temporal-attention layers into every encoder block and into two positions within each decoder resolution stage: the up-sampling block and the final block. We weight each of the four masking tasks defined above as follows: random frame dropout (0.3), block-wise masking (0.25), endpoint interpolation (0.1), and full sequence masking (0.35).

Similar to the coarse image model, a base model embedding dimension of 128 sufficed to model the 2D dataset’s 12 fields. Given the video model’s expanded 124-channel input on the 3D dataset, we increased the UNet width to 256 channels, finding it to converge markedly faster and achieve higher log-likelihood than at 192 channels. The model was trained from scratch like the image model on 32 H100 GPUs, using the same Adam optimizer [Kingma and Ba, 2014] and learning rate of 10^{-4} . It was trained to 2.16M video samples with a batch size of 32.

cBottle-SR The super-resolution model, which performs upscaling from HPX64 to HPX1024 resolution (a factor of 16), is trained within a HEALPix multi-diffusion framework described in 2.2.2. In this setting, the global input data—including latent variables, conditioning fields, and high-resolution targets—are partitioned into spatial patches. Each patch is then independently processed by a local denoising model, which is trained to reconstruct high-resolution content based on temporally and spatially aligned inputs. This approach enables efficient learning of fine-scale features while preserving global coherence through patch-wise training across the full spherical domain.

As illustrated in Figure SI4, this training strategy adapts the standard denoising score matching loss (see Eq. 7) to operate at the patch level. Specifically, the modified objective is defined as

$$\min_{\theta} \mathbb{E}_{\mathbf{x} \sim p_{\text{data}}} \mathbb{E}_{\sigma \sim p_{\sigma}} \mathbb{E}_{\epsilon \sim \mathcal{N}(0, \sigma^2 \mathbf{I})} \mathbb{E}_{i \sim \mathcal{U}} \left\| \Phi_{\theta} \left(\mathcal{F}_i(\mathbf{x}) + \epsilon; \mathcal{F}_i(y), \sigma \right) - \mathcal{F}_i(\mathbf{x}) \right\|^2, \quad (19)$$

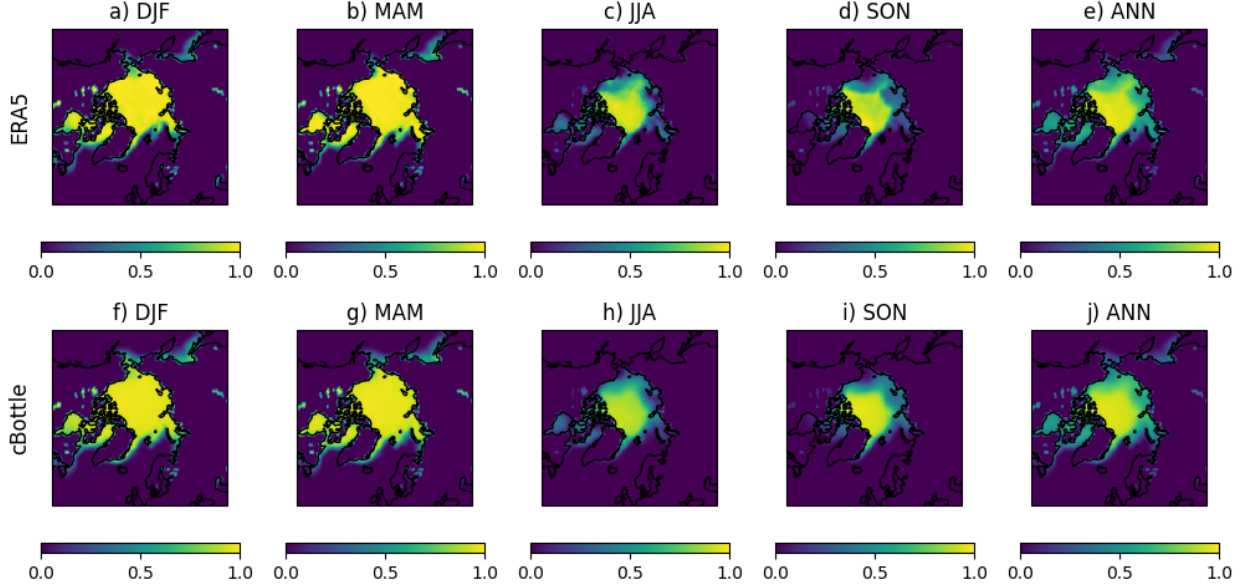


Figure 4: Seasonal cycle of sea ice concentration for ERA5 emulation and ground truth, computed over the test period.

Like `cBottle-3d` we use the Song-UNet with 128 hidden channels. Since it is a local model, we do not need to use the HEALPix padding shown in SI3.

A patch size of 128×128 is used. This is chosen to be much larger than $16\times$ super-resolution factor but is still affordable. To cope with non-stationary spatial features like topography, 20 learnable positional embeddings with a spatial size of HPX1024 grid are introduced and initialized using sinusoidal functions. The inputs of the network consist of (1) the HPX64 data re-gridded bilinearly to the HPX1024 128×128 patch in question, (2) the global position embeddings for this patch, and (4) the global HPX64 data interpolated to the 128×128 lat-lon grid. These are concatenated with the latent before further processing by the encoder. The model was trained to 95520 ICON samples (corresponding to 191 million patches, with repeats) with a batch size of 960. The SGD optimizer was used with a learning rate of 10^{-4} . During training the model uses the log-normal noise distribution of Karras et al. [2022] (p_σ) with $P_{mean} = -1.2$ and $P_{std} = 1.2$. For inference, $\sigma_{max} = 800$.

3 Results

3.1 ERA5 in a Bottle

3.1.1 Variability

A useful generator of climate states should exhibit realistic variability across independent samples from phenomena operating on diurnal, synoptic, seasonal, and interannual time scales that, when averaged, produce a realistic climatology. To assess this we perform an Atmosphere Model Intercomparison Project (AMIP) control run with prescribed monthly-averaged SSTs [Eyring et al., 2016, Gates et al., 1999]. We generate samples every hour from 1940 to 2021 (inclusive). It should be stressed that each atmospheric state is completely independent in each timestep and only shares the same conditioning. This was a large-scale inference, requiring ~ 1024 GPU-hours on the H100 GPU.

We now present a series of common diagnostics used to assess the quality of the generated samples and statistics. Additional analyses are presented in Section G.

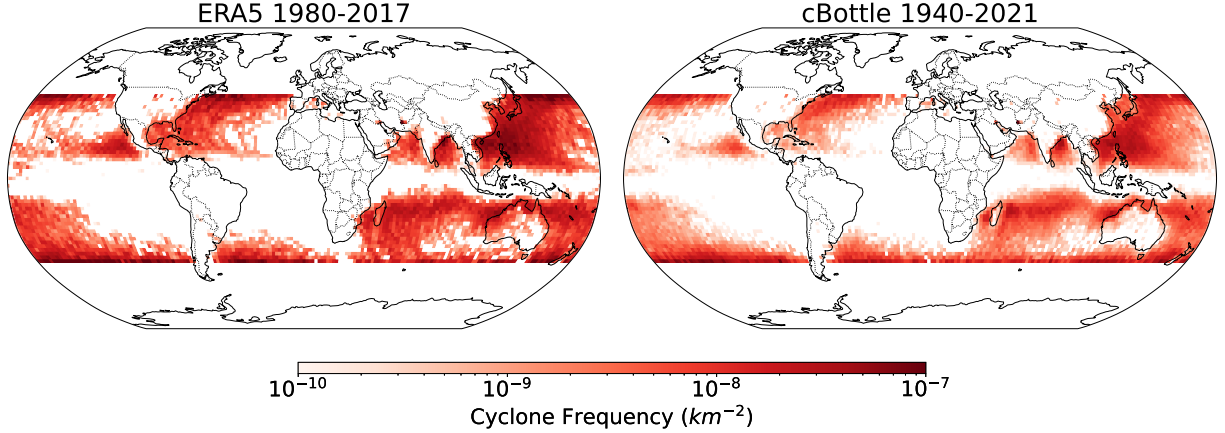


Figure 5: Tropical cyclone occurrence probability derived from ERA5 (1980–2017) and *cBottle* (1940–2021), presented as heatmaps normalized per km^2 .

Climatology and seasonal cycle Figure 4 shows that *cBottle* correctly generates the seasonal evolution of Arctic sea ice concentration. As in the ground truth, generated ice approaches 100% concentration during boreal winter (a,f) and spring (b,g). During boreal summer (c,h) and fall (d,i) the sea ice margin retreats and its concentration is reduced locally over the Beaufort Sea, Chukchi Sea and Bering Sea – poleward of Alaska and Siberia, also reflected in the annual climatology (e,j). These results are evidence that the time-of-year conditioning in *cBottle* works as intended. The seasonal cycle is similarly realistic for other fields (see Figure SI10). The annual mean climate of precipitation of the *cBottle* generated samples also matches the ERA5 and ICON data (see Figure SI11).

Tropical cyclones Consistent with realistic synoptic variability, tropical cyclones are generated in appropriate locations, with appropriate occurrence probability magnitudes (Figure 5). This is assessed using a tracking algorithm based on TempestExtremes v2.1 [Ullrich et al., 2021]. The following filters are applied to identify candidate features: (1) Mean sea level pressure must increase by at least 200 Pa within a 5.5° great-circle distance (GCD) from the candidate point; (2) The difference between geopotential heights at 300 hPa and 500 hPa must decrease by at least $58.8 \text{ m}^2/\text{s}^2$ within a 6.5° GCD; (3) Wind speed must exceed 10 m/s; (4) The latitude of the candidate point must fall within the range of -45° to 45° . As *cBottle* lacks temporal coherence, cyclone detections for both **Target** ERA5 and *cBottle*-ERA5 are computed without temporal continuity tracking to ensure a fair comparison.

Diurnal Cycle The diurnal cycle of rainfall should only be detectable above the noise of other modes of variability in certain subregions of the planet. In Figure 6, we compare the amplitude and signal-to-noise ratio of the diurnal cycle in *cBottle* with ERA5 (see Sec B for details). *cBottle* appears to reproduce even small signals like the locally detectable subtropical stratocumulus drizzle diurnal cycles (see SNR). Moreover, there is a realistic spatial structure of the precipitation diurnal cycle amplitude including spatial details interior to tropical continents – and even the halo that surrounds the Maritime Continent presumably from the emanating diurnally phased convection propagation there. See the SI Fig SI1 for the same analysis with surface air temperature.

3.1.2 Northern Annular Mode

We next assess a planetary scale mode of internal variability. In the northern hemispheric midlatitudes, the Northern Annular Mode is the leading empirical orthogonal function (EOF), which accounts for one-fifth of overall variance in the 1000 hPa geopotential height (REF). Figure 7 shows that the leading EOF computed from *cBottle* generations exhibits the expected spatial structure of the NAM as well as percent variance explained. Moreover, Figure 8 shows that the daily variability of *cBottle*’s NAM is realistically large and

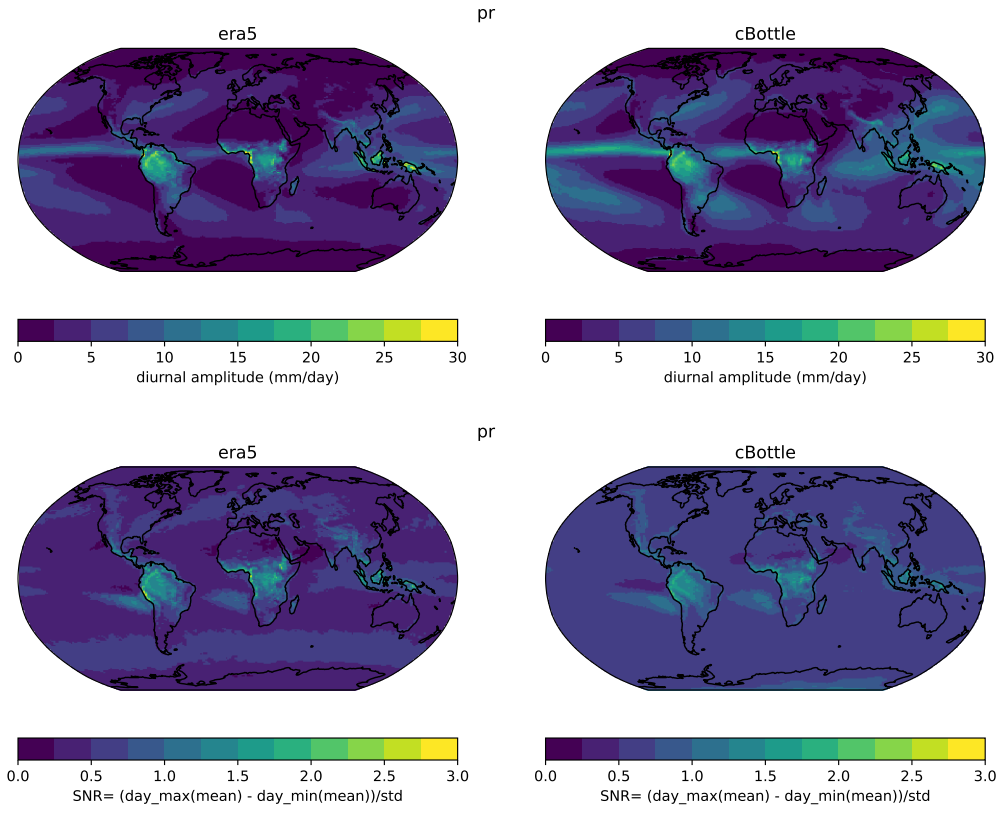


Figure 6: Diurnal cycle diagnostics for surface precipitation. (top row) Amplitude of the diurnal cycle. (bottom row) signal to noise ratio.

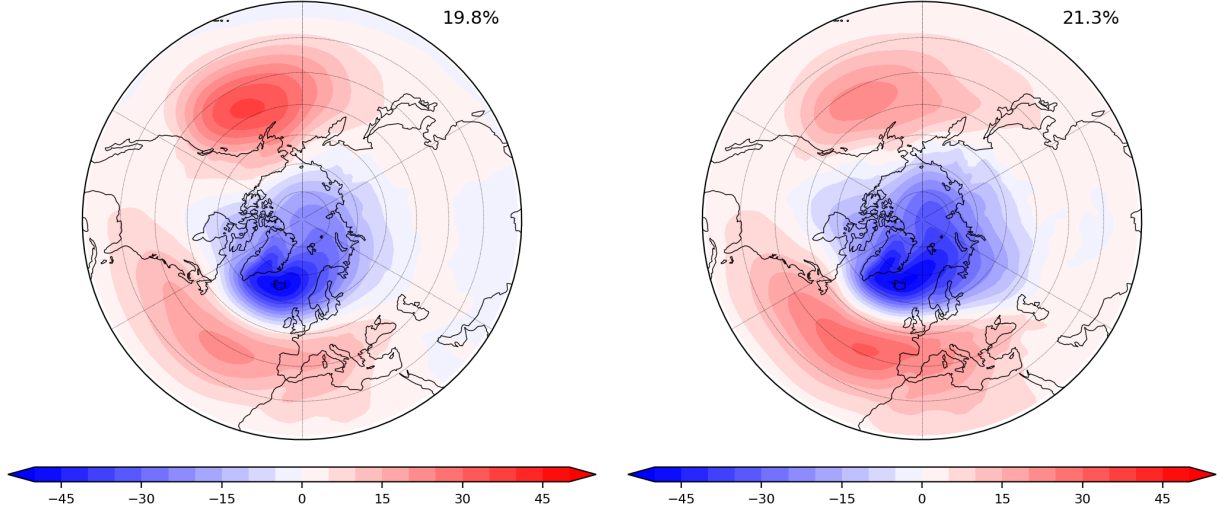


Figure 7: Arctic Oscillation or the Northern Annular Mode (NAM) computed based on Nov-Apr Z1000 monthly mean anomalies. Text overlay indicates the percentage of the total variance attributed to the plotted EOF mode. (left) *cBottle*. (right) ERA5. Computed over 1970-2010.

even contains a low frequency envelope that is in phase with interannual fluctuations in the ERA5 NAM state, suggesting learnt associations between the generated NAM state and the SST input to *cBottle*.

3.1.3 ENSO Variability

Appropriate conditioning on SST is confirmed by focusing on the El Nino Southern Oscillation (ENSO). Figure 9 demonstrates that *cBottle* produces realistic ENSO precipitation variability, measured as the regression of its generated precipitation against the Nino3.4 index associated with its input SST. Within the tropics, increases of Central Pacific precipitation during the positive phase of ENSO associate with reductions of generated precipitation over tropical Africa, Indonesia and South America, consistent with Walker Cell modulation. These results add to the evidence of the *cBottle*’s ability to condition generated variability appropriately on SST, in addition to time of year and time of day.

3.1.4 Non-stationarity: Heat waves

Figure 10 shows the secular trends in global mean quantities for ERA5 and *cBottle*. *cBottle* noticeably misses the climate change trend in surface fields (temperature and precipitation), but does better for tropospheric quantities like Z500. Taking this caveat, we opt to use Z500 to analyze the trend in extreme heat—this is reasonable since surface heat waves are often linked to anomalous Z500 at atmospheric blocking patterns. For example, the 2021 Pacific Northwest heat wave feature +4 standard deviation height anomalies [Mass et al., 2024]. *cBottle* is able to reproduce observed trends in the occurrence of heights exceeding the 90th percentile in space (Figure 10e,f), albeit with reduce amplitude in some regions. The land averaged trends are also quite similar (Figure 10d).

3.2 ICON in a bottle

Generation of ICON states at HPX1024 resolution is achieved through a two-stage process in which the macroscale generator of the ICON modality at HPX64 is fed through a patch-based super-resolution module (see Section 2.7.2), which we assess below.

All super-resolved results presented here are produced using a consistent configuration: a maximum noise level (σ_{max}) of 800, 18 sampling steps, and $S_{churn}=0$.

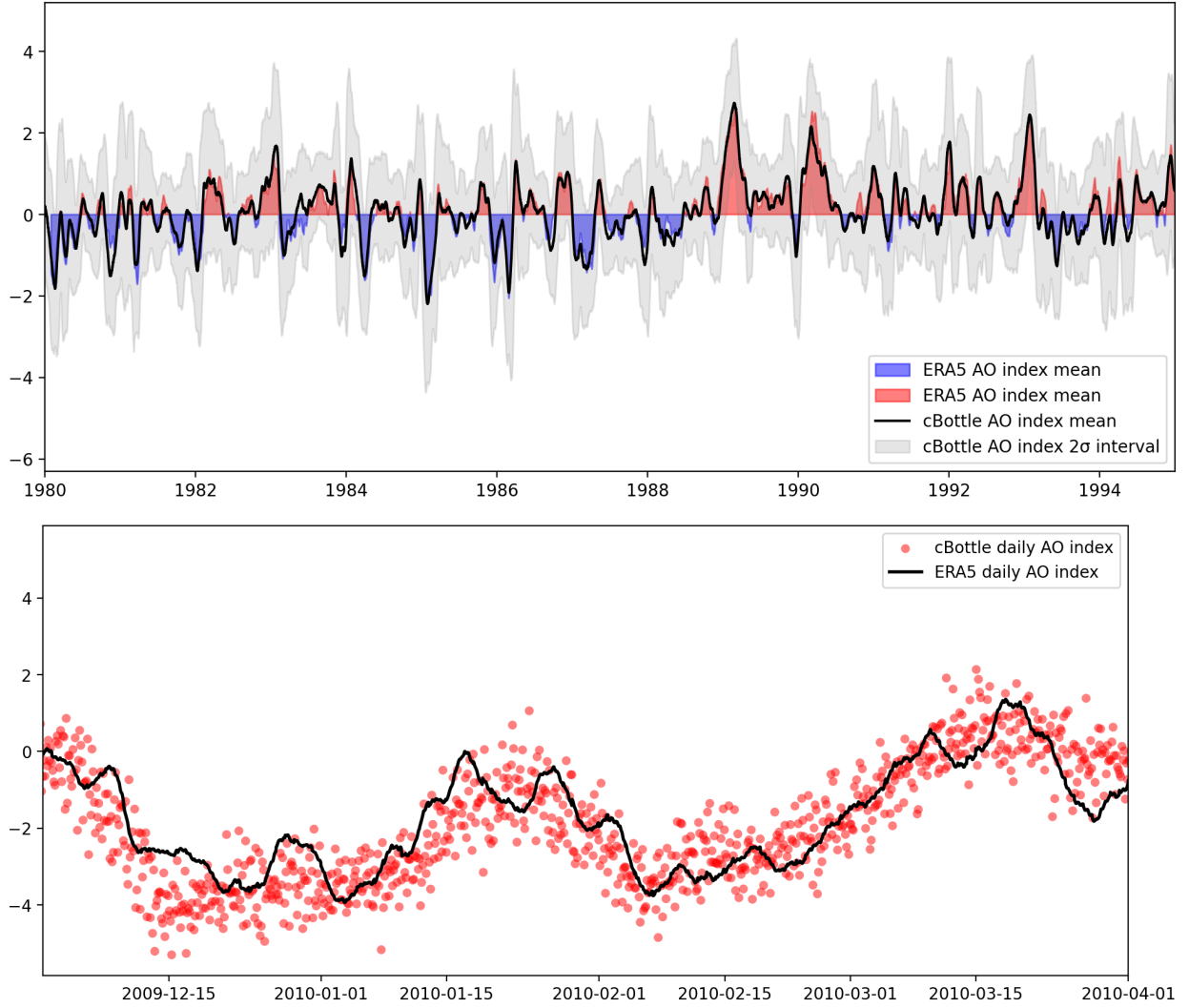


Figure 8: Arctic Oscillation or the Northern Annular Mode (NAM) daily indices between 1980 and 1995 computed as projections of daily Z1000 anomalies onto the ERA5 NAM mode. Top - Red/Blue filled curves: ERA5 3 month running mean, solid black line: *cBottle* 3 month running mean, grey filled region: *cBottle* $\pm 2\sigma$ interval around the mean. Bottom - Solid line: ERA5 daily AO index, red circles: *cBottle* daily AO index.

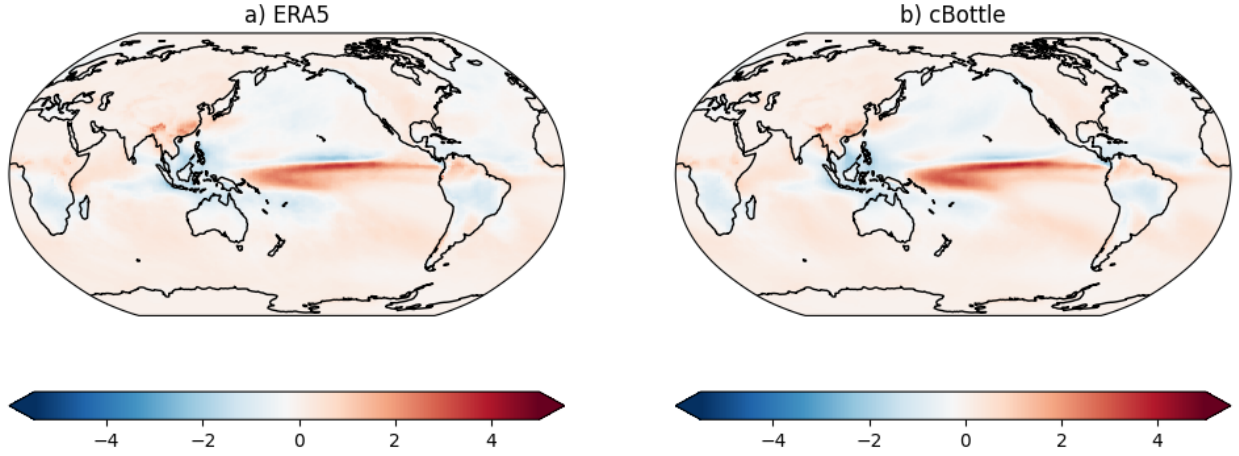


Figure 9: El Niño-Southern Oscillation. Regression coefficient of the Nino3.4 index against monthly average precipitation. (left) ERA5. (right) Climate in a bottle. Computed over 1990-2020 inclusive.

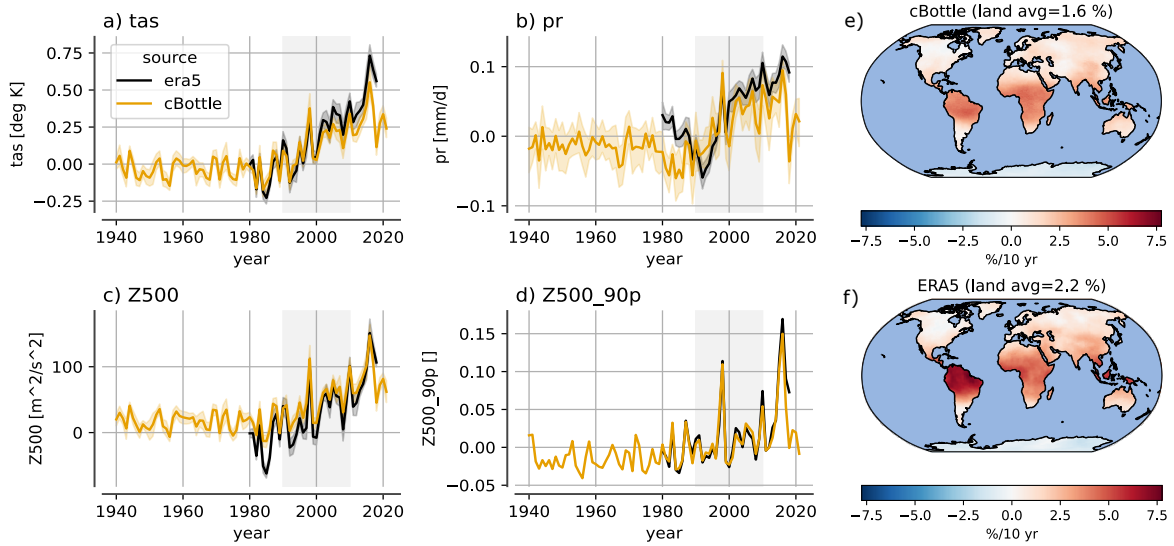


Figure 10: Time series of global mean anomalies from ERA5's monthly climatology computed over 1980-2010. (a) surface air temperature, (b) precipitation, (c) 500-mb geopotential. 95% confidence-intervals for the annual mean anomaly are computed by bootstrapping over the monthly averages. (d) change in probability of exceeding 90-percentile of Z500 (Z500-90p) computed for 1990-2010 for all land points. Also shows Z500-90p trend maps for cBottle-ERA5 (e) and ERA5 (f).

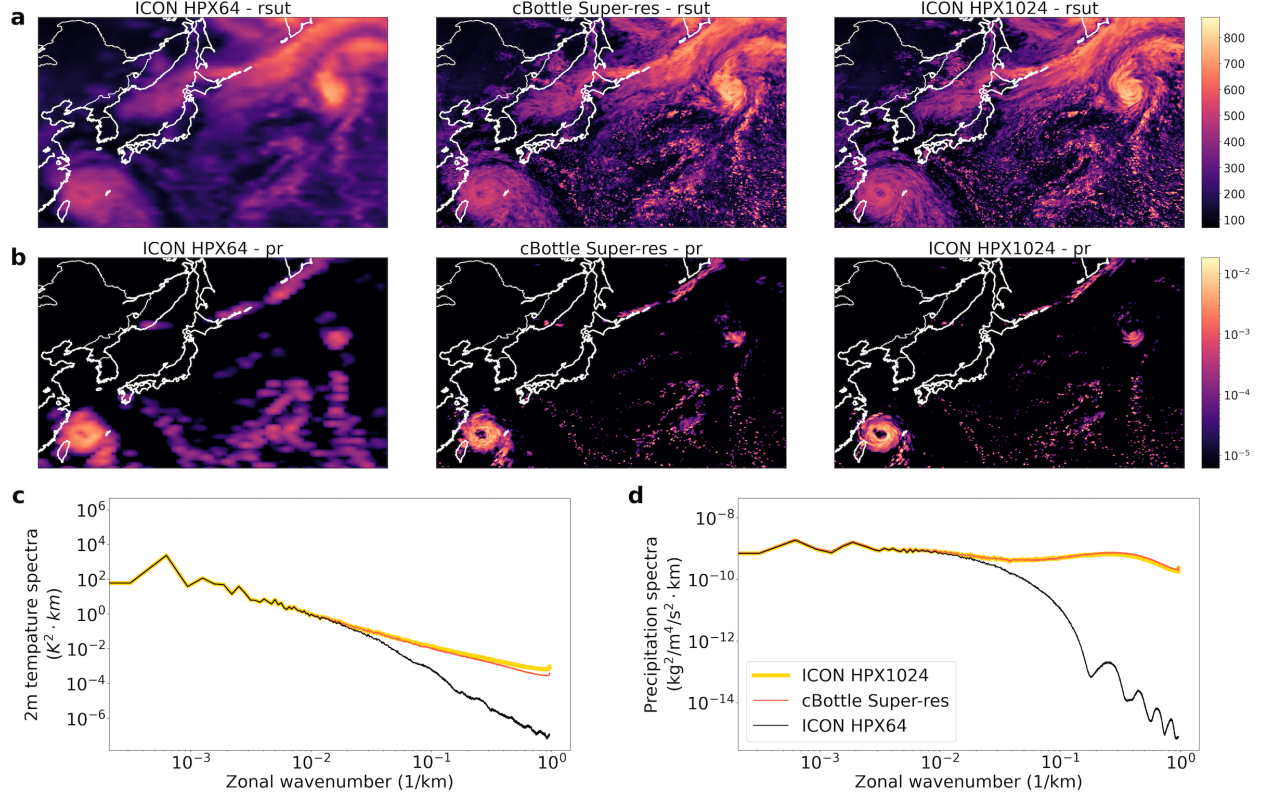


Figure 11: (a), (b) Demonstration of super-resolved atmospheric variables outgoing shortwave radiation, and precipitation flux of ICON HPX64 at a selected time during an extreme tropical cyclone event and adjacent midlatitude front. From left to right are the input ICON HPX64, HPX1024 super-resolved by cBottle, and ICON HPX1024. (c), (d) Spherical power spectra plots for 2-meter temperature and precipitation of ICON HPX64 super-resolution inferences across 32 validation samples.

3.2.1 Super-Resolution Results

Figure 11 (a), (b) provides a first qualitative assessment of the super-resolution. Here we choose a convenient time sample from the test set, in which a West Pacific tropical cyclone occurred adjacent to a large midlatitude weather system to its northeast. The performance of super-resolution is shown for two field variables – upwelling solar radiation (first row) and precipitation rate (second row). Compared to the ground truth (right column), the results (middle column) are generally encouraging. For the tropical cyclone, appropriate orographic maximization of convection over the interior of Taiwan – not present in the macroscale inputs (left column) – is realistically generated. So too are details of the eyewall structure and surrounding rain bands, albeit with less spatial coherence than in the ground truth. Meanwhile, for the midlatitude weather system, a plausible fine-scale frontal band is generated, extending from the Kiril islands to just east of the Kamchatka peninsula, with consistent horizontal scale and position as the ground truth, across both field variables.

A more quantitative assessment is shown in Figure 11 (c), (d) from the view of spectra. The plots are generated using 32 randomly selected samples spanning from March 6, 2024, to July 23, 2025. The spherical power spectra are computed by averaging the squared magnitudes of the spherical harmonic coefficients over the azimuthal index m and across the temporal dimension. Correct distribution of variance as a function of spatial scale is confirmed in the power spectra for temperature and precipitation.

3.2.2 End-to-end synthesis

We now turn to results from our capstone task of attempting to generate 12M-pixel multivariate ICON states purely from noise, time of year, time of day, and a monthly mean map of SST. The left column of Figure 12 (a), (b), (c), (d) provides a qualitative demonstration of the results (see also Figure 1). Results are shown for an arbitrary subregion spanning the entire North Pacific ocean, across four arbitrary time periods having distinct weather states. It is important to note that the ground truth (corresponding right columns) should not be compared to the model output for any matched spatial positioning of individual weather events, since the task is unconditional generation. That is, the ground truth also has distinct weather states. Rather, what is noteworthy in the comparison is the common modulation of similar microscale weather detail by variably positioned macroscale weather events.

From this view, we find encouraging co-generation of outgoing shortwave radiation and precipitation channels. As in the ground truth, sub-sectors of midlatitude eddies exhibit km-scale organization patterns of non-precipitating shallow cloud (i.e. evident in the shortwave channel but not the precipitation channel). As in the ground truth, zonally elongated macroscale filaments of the intertropical convergence zone are embedded with fine-scale precipitation having its own characteristic length scale of organization. In contrast, midlatitude precipitation is comparatively stratiform – lower intensity and more spatially coherent – with the exception of fronts visible in both brightness and rainfall. While difficult to summarize statistically, such multi-scale, multi-variate spatial associations are readily visible to the trained human eye accustomed to inspecting weather data, and suggest successful synthesis.

Spectra analysis again quantitatively confirm this finding (Figures 12 (e), (f)). On the one hand, secondary imperfections are introduced that were not apparent when super-resolution is used in isolation of macro-scale generation (Figures 11 (c), (d)) such as too low occurrence of the very coldest surface temperatures on the planet (less than -60 Centigrade). On the other hand such imperfections are minor such that the results are overall of reasonable enough quality so as to suggest the viability of cascaded super-resolution as a means to generate multivariate ICON states. Figures 12 (e), (f) are generated using 64 randomly selected samples spanning from March 6, 2024, to July 23, 2025.

3.2.3 Video diffusion

Spatio-Temporal Analysis To evaluate whether the video diffusion model captures realistic atmospheric dynamics through time—beyond just generating independent plausible snapshots—we analyze its ability to reproduce the patterns characteristic of mid-latitude storm track evolution in Figure 13. Following the approach of [Rao et al., 2002], we compute one-point lag correlation maps on mean sea level pressure. The video model generations successfully reproduce both the spatial structure of these patterns and their temporal evolution at comparable propagation speeds to the ICON ground truth. At negative lags, we observe a coherent wave train approaching the reference point from the west, and at positive lags, these correlation continue propagating eastward. The model’s ability to replicate these spatio-temporal patterns indicates the temporal attention mechanism enables the model to capture the underlying physical dynamics and generate coherent trajectories of atmospheric state.

3.2.4 Ablations

Noise schedule Figure 14 demonstrates the impact of noise schedule choice on diffusion models for atmospheric data. The bottom row shows results using a log-normal schedule ($P_{mean} = -1.2$, $P_{std} = 1.2$) typically used for image generation [Karras et al., 2022]. This schedule introduces insufficient noise to mask the the dominant diurnal cycle of outgoing shortwave radiation during training. Consequently, the model learns to detect and amplify residual signal patterns from noised inputs rather than using the time-of-day conditioning. However, during inference where starting from pure noise provides no such signal to extract, the model produces physically inconsistent results. Panel (g) shows this most clearly, with a “double sun” artifact with radiation appearing in multiple incorrect locations.

In contrast, the log-uniform schedule (top row) with higher σ_{max} provides sufficient noise to completely obscure the diurnal pattern during training, forcing the model to learn the relationship between time-of-day conditioning and the spatial distribution of solar radiation. This yields physically consistent results

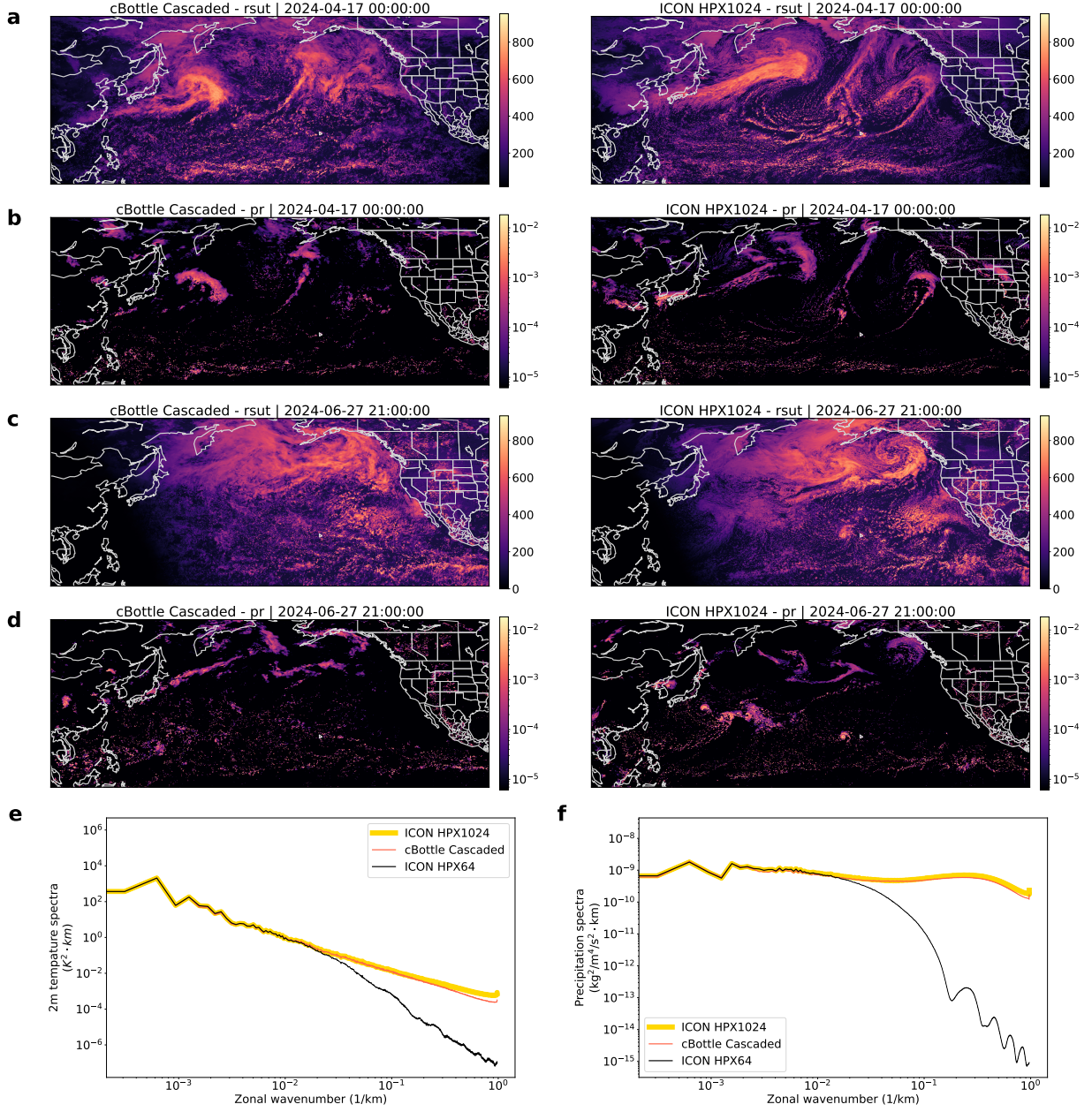


Figure 12: (a-d) Demonstration of 2 HPX1024 samples from cascaded cBottle, showing outgoing shortwave radiation, and precipitation flux. Samples from cascaded and ICON are not matched. (e), (f) Spherical power spectra of cascaded cBottle inferences across 64 validation samples, for 2-meter temperature and precipitation.

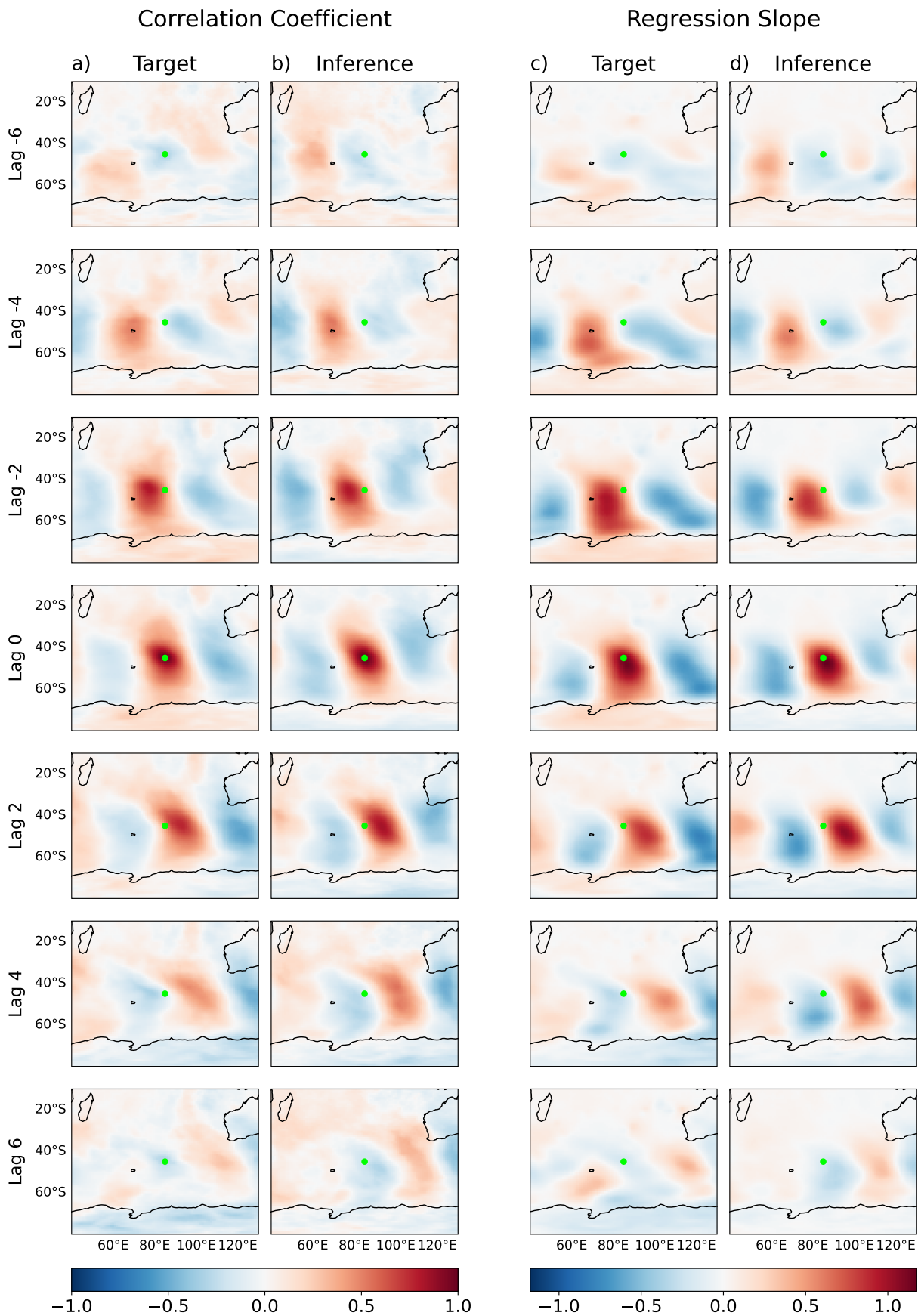


Figure 13: Lagged correlation (left) and regression slope (right) maps for mean sea level pressure computed on unconditional video model generations and ICON ground truth. Maps are computed relative to a seed point at 45°S, 85°E (green dot), and averaged over 60 non-overlapping 3-day sequences from December to May.

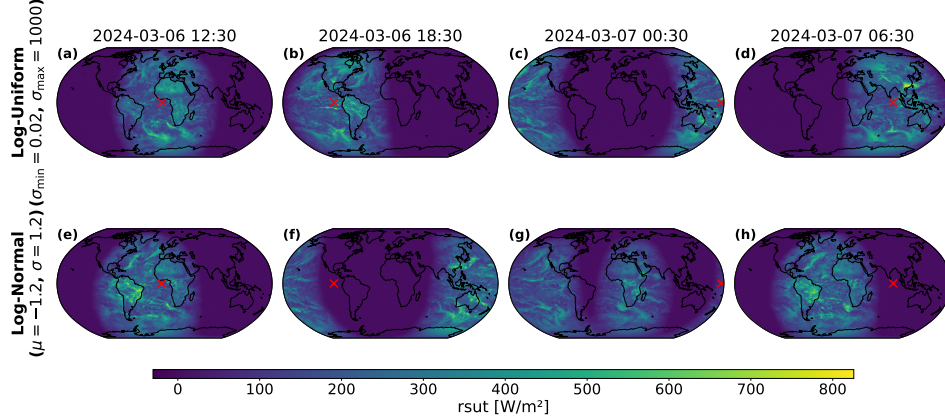


Figure 14: Four consecutive frames of reflective visible light (rsut) from a sequence generated by video diffusion models trained with either a log-uniform (top) or log-normal (bottom) noise schedule. Generations are conditioned on the calendar embedding and monthly average SST. Red \times marks indicate the subsolar point at each timestep.

qualitatively with correctly positioned subsolar points. This visual comparison confirms the earlier theoretical argument (see Subsection 2.4) that atmospheric variables, some with planetary scale patterns, require substantially higher noise ceilings than is standard for diffusion to avoid *signal leak bias*.

Training data size ablation Figure 15 illustrates the spherical power spectra of inference results from two models trained on datasets of differing sizes: one with 3.75 years of distinct samples (72,360 in total), and another with 4 weeks of distinct samples (1,344 in total), with each week randomly selected from a different season to ensure representative temporal coverage. Both models were trained using 95,000 total samples via repetition to match training iterations.

Across almost all variables, the **4 weeks** model closely reproduces the spectral characteristics of the **3.75 years** model. This alignment is particularly notable given the drastic reduction in training data diversity. The only substantial deviation appears in the precipitation spectra, where the **4 weeks** model exhibits slightly lower zonal energy at high wavenumbers, suggesting a modest underrepresentation of fine-scale variability. These results demonstrate the model’s strong data efficiency: even when trained on a small, seasonally representative subset, it retains robust downscaling performance and preserves key spectral structures across a range of physical variables.

3.3 Multimodal

In this section we demonstrate how the separate modalities and generative vs. super-resolution modules of *cBottle* can be composed into novel workflows, providing the beginnings of a foundational versatility.

3.3.1 ICON-Informed Downscaling of ERA5

Although the super-resolution model is trained exclusively on ICON data, it demonstrates zero-shot generalization capability when applied to data from other sources. In this subsection, we assess its skills on ERA5 data regridded to HPX64 resolution. The corrupted radiation channels in ERA5 have been infilled using the method described in Section 3.3.2. The resulting super-resolved outputs are compared against both the 3-km High-Resolution Rapid Refresh (HRRR) dataset over CONUS and the native-resolution ICON model at HPX1024. All datasets used in this evaluation are regridded to a common 3-km Lambert conformal projection over the CONUS region to ensure fair spatial alignment.

Figures 16 (a), (b), (c) presents a qualitative comparison of three representative variables: 10-meter eastward wind velocity, outgoing shortwave radiation, and precipitation rate. The figure shows spatial subsets spanning the Midwest to the Eastern United States, with four columns corresponding to the original

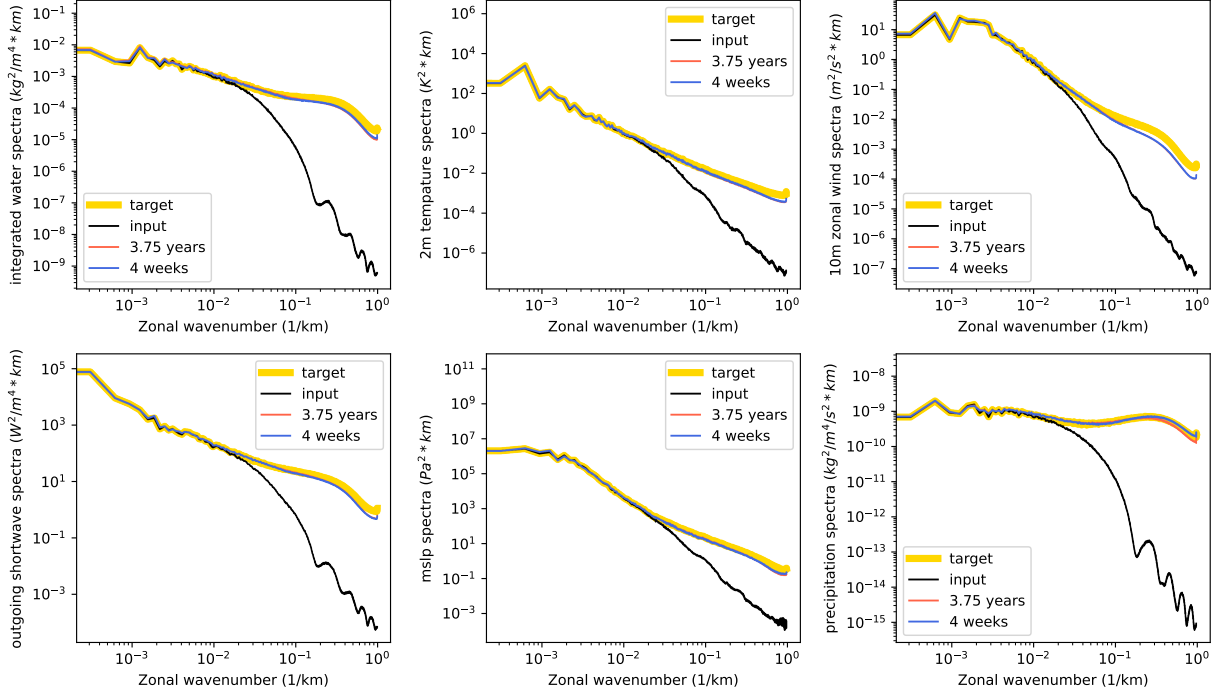


Figure 15: Training data size ablation study: Power spectra from global super-resolution models trained on 3.75 years versus 4 weeks of timesteps.

ERA5 HPX64 input, the super-resolved ERA5 output generated by our model, the HRRR reference, and the ICON HPX1024 reference. Note that the ICON simulation is a free-running model and is not temporally aligned with the ERA5 or HRRR data; however, it still serves as a useful reference for assessing small-scale structural similarity. While the large-scale patterns in the super-resolved ERA5 resemble those in the original ERA5 and HRRR data, the finer-scale structures more closely resemble those in the native-resolution ICON fields. This suggests that the model effectively emulates high-frequency features in ICON and is capable of generating high-resolution patterns and dynamics that are not explicitly present in the coarse-resolution data.

The zonal-mean spherical power spectra for four representative variables are shown in Figure SI9 (d), (e): 2-meter temperature, outgoing shortwave radiation, and precipitation. Comparisons are made across five datasets: the ERA5 HPX64 input, the super-resolved ERA5 output generated by our model (*cBottle*), the HRRR reference, ICON at HPX64, and ICON at HPX1024 resolution.

For variables where ERA5 HPX64 and ICON HPX64 exhibit similar spectral characteristics—such as kinetic energy and temperature—the super-resolved outputs from *cBottle* closely follow the spectral slope and amplitude of the ICON HPX1024 reference, indicating successful reconstruction of high-frequency content. This alignment demonstrates the model’s capacity to synthesize physically plausible fine-scale variability.

For channels where the ERA5 HPX64 input exhibits significant spectral differences from the ICON HPX64 input (precipitation), however, the model’s ability to recover fine-scale variability is limited. While *cBottle* partially bridges the gap, it underrepresents high-wavenumber energy relative to ICON HPX1024 and HRRR. This highlights the challenge of zero-shot generalization when there is a domain shift in spectral characteristics between the training and evaluation inputs.

To sum up, it is encouraging to observe that the super-resolution model can effectively super-resolve unseen data in a zero-shot setting, while also faithfully emulating the characteristics of its training data. Reducing spectral and distributional discrepancies caused by domain shifts—potentially through the inclusion of more diverse training datasets—may further improve the model’s robustness and enhance its applicability in climate science.

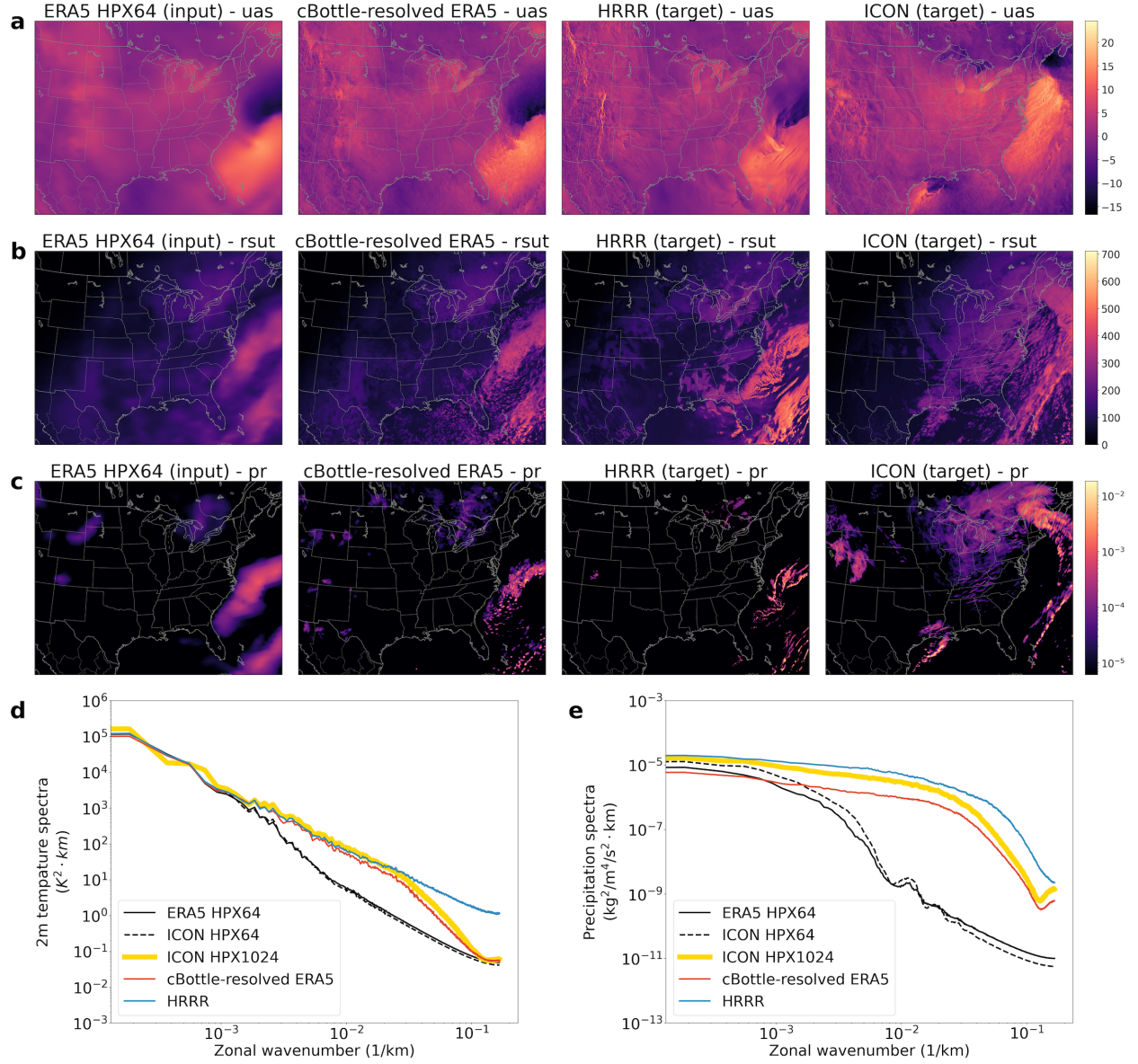


Figure 16: (a), (b), (c): Illustration of the super-resolved ERA5 output at 15:00 UTC on December 11, 2018, with radiative channels infilled using the *cBottle* HPX64 generator. The first three columns correspond to the same timestamp, while the rightmost column (ICON) shows the free-run forecast for 15:00 UTC on December 11, 2024. From top to bottom, the rows represent 10-meter eastward wind velocity, outgoing shortwave radiation, and precipitation. (d), (e) Power spectra of *cBottle*-resolved ERA5 and various baselines, computed over 10 samples. All datasets are regridded to a Lambert-Conformal projection for comparison. ERA5, *cBottle*-resolved ERA5, and HRRR share an identical set of evaluation timestamps. ICON HPX64 and ICON HPX1024 use matching times of day and days of the year, but from different years.

3.3.2 Channel filling

Following Appendix I.2 of Song et al. [2020b], let $\Omega : \mathbb{R}^{C \times \mathbf{d}} \rightarrow \mathbb{R}^{C_K \times \mathbf{d}}$ and $\bar{\Omega} : \mathbb{R}^{C \times \mathbf{d}} \rightarrow \mathbb{R}^{C_U \times \mathbf{d}}$ denote the slicing operators that extract the known and unknown channels, respectively, where \mathbf{d} denotes an arbitrary set of additional dimensions (e.g., spatial or temporal). The unknown subset at sampling time t is then denoted by $\mathbf{z}_t = \bar{\Omega}(\mathbf{x}_t)$. The conditional score function required to impute the missing channels can be approximated as

$$\nabla_{\mathbf{z}} \log p(\mathbf{z}_t | \Omega(\mathbf{x}_0), \sigma_t) \approx \nabla_{\mathbf{z}} \log p([\mathbf{z}_t; \Omega(\mathbf{x}_t)] | \sigma_t), \quad (20)$$

where $[\cdot; \cdot]$ denotes concatenation along the channel dimension.

To evaluate the imputation capability of the model, we focus on infilling radiation channels in the ERA5 and ICON datasets. Specifically, the imputed variables include outgoing shortwave radiation, outgoing longwave radiation, and surface downwelling shortwave radiation. Figure 17 visualizes the infilled outgoing shortwave radiation for both ERA5 and ICON, as produced by the proposed *cBottle* framework. All ICON images (**Target** ICON, **cBottle-Infill** ICON, and **cBottle** ICON) correspond to the same timestamp, as do all ERA5 samples.

Compared to the respective ground truths, *cBottle* successfully reconstructs plausible radiation structures for both ERA5 and ICON. The contrast between **cBottle-Infill** ICON and **cBottle** ICON is particularly illuminating: although both are conditioned on identical information (timestamp, day of year, and SST), only the result from the infilling workflow (**cBottle-Infill** ICON) shows accurate reconstruction of the missing radiation channels in alignment with the **Target** ICON. This highlights that the improvement arises from the imputation technique itself, rather than from conditioning alone.

Furthermore, *cBottle* with channel filling proves effective in mitigating dataset-specific artifacts. For instance, as seen in the comparison between **cBottle-Infill** ERA5 and **Target** ERA5, the model reproduces coherent structures and dynamics while simultaneously removing the streaking artifacts inherent in the original ERA5 fields.

In summary, these results demonstrate that the imputation approach employed by *cBottle* not only enables the plausible reconstruction of missing physical variables, but also helps mitigate known deficiencies in climate datasets. This underscores the potential of *cBottle* as a valuable tool for data recovery in atmospheric science, particularly in scenarios where observational records are incomplete, corrupted, or degraded by systematic artifacts.

3.3.3 Bias correction

This approach takes advantage of the latent representation of the diffusion model. To transition a sample from dataset i to j we evaluate the ODE forward to get the latent then reverse it with the β -denoiser.

It may seem surprising that this yields a realistic sample. Liu et al. [2022] explain that since the flow defined by an ODE is unique, the trajectories between samples cannot cross one another. This property makes the flow map close to an optimal transport map between the distributions.

Figure SI15 shows that *cBottle* can debias the cloud field of the original ICON data while maintaining temporal coherence across frames. The ICON model prefers a liquid-heavy partitioning between cloud water and ice compared to ERA5 (cf Fig. 18). It has nearly the double the liquid water as ERA5. Overall, the location of the clouds in the bias corrected ICON data is similar, though there are some apparent differences.

Overall, the ability to translate between datasets with a single foundation model is an exciting potential application, and we leave more detailed analysis to future studies. Unlike Liu et al. [2022] our model is not trained explicitly to map from one dataset to the other. That approach would require training a separate model for each pair of datasets so does not scale well to many different data sources. By training one model on all potential datasets, we can use the denoiser to define a shared latent space, a desirable property of a foundation model.

4 Conclusions

We have demonstrated that masked denoising diffusion is a feasible approach to generative modeling of the atmosphere. The two-stage cascade comprises: (i) a coarse-resolution multi-modal climate data generator;

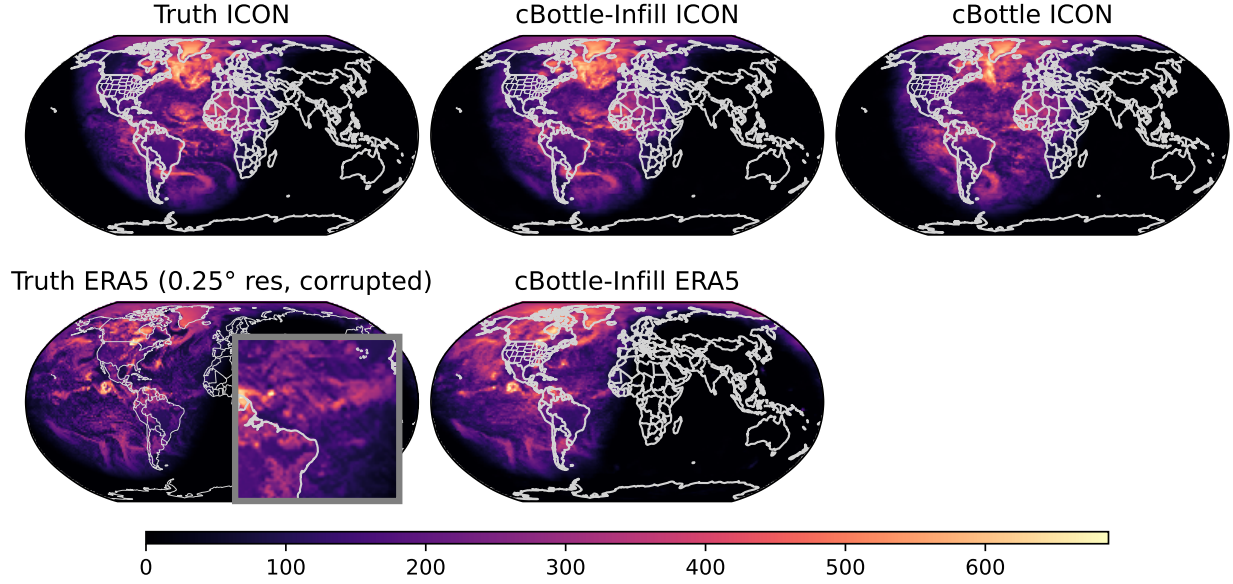


Figure 17: Imputation of outgoing shortwave radiation using *cBottle*. *cBottle-Infll* ICON: ICON data with radiation channels masked and subsequently reconstructed via *cBottle*. *cBottle* ICON: ICON data fully generated by *cBottle* using only SST and timestamp as conditioning. **Target** ERA5: ERA5 reference with native spatial resolution and known streaking artifacts. *cBottle-Infll* ERA5: ERA5 data with radiation channels infilled by *cBottle*.

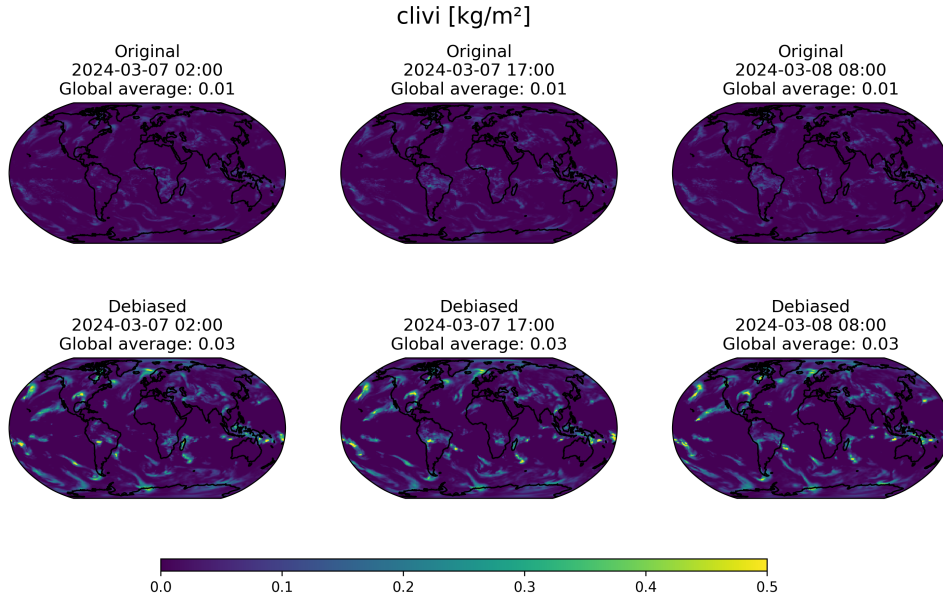


Figure 18: Bias correction of the total cloud ice.

and (ii) a cascaded patch-based super-resolution module. Together, these have the potential to enhance: (i) the way km-scale climate data is accessed; and (ii) the practice of climate informatics.

In the first stage, provided only 200 kb of inputs comprising two scalars (time of year, time of day) and a 50,000 pixel map of monthly mean SST data, *cBottle* synthesizes 9 MB of global multivariate samples for 45 channels that emulate the macroscale (HPX64) climatological properties of ERA5 or ICON. Our analysis suggests the generated samples exhibit the same mean state and variance from diurnal, synoptic, seasonal and interannual modes of variability as the ground truth. In the second stage, given such HPX64 fields, *cBottle*’s cascaded super-resolution module generates HPX1024 states for 12 channels, totaling 600 MB. This stage exploits a patch-based approach to handle scaling to the global (12.5-million pixel) domain. We have shown that the super-resolved states have accurate spectra, can be trained with remarkable sample efficiency – as little as four weeks of ICON HPX1024 output – and that secondary patch boundary artifacts can be mostly controlled using simple overlap techniques. Either stage can be used independently, for instance, to generate coarse-resolution (HPX64) climate samples, or to super-resolve existing HPX64 climate data to HPX1024 resolution with ICON-learned high-resolution characteristics.

The resulting end-to-end system – ICON in a bottle — offers 3000x compression ratio per sample over the raw data (256x compression ratio per channel for 12 channels). We suggest this technology can thus greatly reduce the bottleneck that storage, I/O, and data movement presents in modern informatics, which has become especially extreme with the advent of global cloud resolving simulation output. This end-to-end system enables users to access realistic km-scale data not by high-latency retrieval of stored data but by low-latency generation of that data, on demand, from a generative ML model.

Moreover, the modular and multi-modal nature of *cBottle* demonstrates new possibilities characteristic of AI foundation modeling that are as yet unfamiliar to the climate science community under the prevailing autorogressive paradigm for emulation. *cBottle* exploits climate information across the multiple modalities it is trained on, and transfers learnings across them. For instance, we have shown how high-resolution textures of ICON-learned cloud-scale organization can be in-painted onto the appropriate sectors of synoptic systems of the macroscale ERA5 modality. We have also shown how channels missing from one-modality can be readily transferred from another, by in-painting the missing shortwave radiation field in the ERA5 modality exploiting what was learnt from ICON. The narrow lesson is that synthetic output from high-resolution simulations can be used more flexibly than it might otherwise appear. The broader lesson is more profound: While our proof of concept has focused on just two data modalities for simplicity, we hope it inspires extensions across the many complementary observing and simulating systems of the Earth System, where such cross-modal learning, in-filling, mode-transfer, and bias-correction becomes increasingly useful for climate science and society. We expect these extensions to help realize a climate foundation model at the km-scale.

In terms of methodology, we have introduced diffusion on the HEALPix grid and highlight the importance of the noise schedule when training denoising diffusion models on scientific data. In particular we show that the defaults most often used in natural image generation literature are not capable of generating extremely large-scale modes like the seasonal and diurnal cycles. Fixing this required two main innovations: i) increasing the range of noise levels sampled during training and inference; and ii) adding appropriate time and position embedding. Specifically, we propose tuning the noise schedule based on spectral analysis of the data, and show that the noise schedule should scale with \sqrt{n} where n is the size of the largest-scales modes in number of scalars (pixels \times channels). This perspective should be helpful to anyone training diffusion models on scientific data.

Additional limitations of our preliminary work are important to note. Non-stationary trends are not optimally represented in the current version of *cBottle*; while we have demonstrated that 90th percentile 500 hPa geopotential height exceedance trends can be emulated, analogous trends in surface temperature are currently elusive. The mean climate – while reasonable – is imperfect, including 4-10% biases in the zonal mean precipitation rate. Another important limitation is that our image generation framework cannot diagnose the duration of events or commonly used metrics like the return time of an event. Future work will need to add temporal coherence and extend the system to enable the generation of spatio-temporally coherent time series of phenomena.

References

- Omer Bar-Tal, Lior Yariv, Yaron Lipman, and Tali Dekel. Multidiffusion: Fusing diffusion paths for controlled image generation, 2023. URL <https://arxiv.org/abs/2302.08113>.
- Seth Bassetti, Brian Hutchinson, Claudia Tebaldi, and Ben Kravitz. Diffesm: Conditional emulation of temperature and precipitation in earth system models with 3d diffusion models. *Journal of Advances in Modeling Earth Systems*, 16(10):e2023MS004194, 2024.
- Peter Bauer, Bjorn Stevens, and Wilco Hazeleger. A digital twin of earth for the green transition. *Nature Climate Change*, 11(2):80–83, 2021. doi: 10.1038/s41558-021-00986-y. URL <https://www.nature.com/articles/s41558-021-00986-y>.
- Kaifeng Bi, Lingxi Xie, Hengheng Zhang, Xin Chen, Xiaotao Gu, and Qi Tian. Accurate medium-range global weather forecasting with 3D neural networks. *Nature*, 619(7970):533–538, July 2023. ISSN 0028-0836,1476-4687. doi: 10.1038/s41586-023-06185-3.
- Andreas Blattmann, Robin Rombach, Huan Ling, Tim Dockhorn, Seung Wook Kim, Sanja Fidler, and Karsten Kreis. Align your latents: High-resolution video synthesis with latent diffusion models, 2023. URL <https://arxiv.org/abs/2304.08818>.
- Cristian Bodnar, Wessel P Bruinsma, Ana Lucic, Megan Stanley, Johannes Brandstetter, Patrick Garvan, Maik Riechert, Jonathan Weyn, Haiyu Dong, Anna Vaughan, Jayesh K Gupta, Kit Tambiratnam, Alex Archibald, Elizabeth Heider, Max Welling, Richard E Turner, and Paris Perdikaris. Aurora: A foundation model of the atmosphere. *arXiv [physics.ao-ph]*, May 2024.
- Matthew Chantry. Personal communication. Personal communication, 2024. Conversation on September 11, 2024.
- William E Chapman, John S Schreck, Yingkai Sha, David John Gagne, II, Dhamma Kimpara, Laure Zanna, Kirsten J Mayer, and Judith Berner. CAMulator: Fast emulation of the community atmosphere model. *arXiv [physics.ao-ph]*, April 2025.
- Ting Chen. On the importance of noise scheduling for diffusion models. *arXiv [cs.CV]*, January 2023.
- Nathaniel Cresswell-Clay, Bowen Liu, Dale Durran, Zihui Liu, Zachary I Espinosa, Raul Moreno, and Matthias Karlbauer. A deep learning earth system model for efficient simulation of the observed climate. *arXiv [physics.ao-ph]*, September 2024.
- Martin Nicolas Everaert, Athanasios Fitsios, Marco Bocchio, Sami Arpa, Sabine Süsstrunk, and Radhakrishna Achanta. Exploiting the signal-leak bias in diffusion models. *arXiv [cs.CV]*, September 2023.
- Veronika Eyring, Sandrine Bony, Gerald A Meehl, Catherine A Senior, Bjorn Stevens, Ronald J Stouffer, and Karl E Taylor. Overview of the coupled model intercomparison project phase 6 (CMIP6) experimental design and organization. *Geosci. Model Dev.*, 9(5):1937–1958, May 2016. ISSN 1991-959X,1991-9603. doi: 10.5194/gmd-9-1937-2016.
- W Lawrence Gates, James S Boyle, Curt Covey, Clyde G Dease, Charles M Doutriaux, Robert S Drach, Michael Fiorino, Peter J Gleckler, Justin J Hnilo, Susan M Marlais, Thomas J Phillips, Gerald L Potter, Benjamin D Santer, Kenneth R Sperber, Karl E Taylor, and Dean N Williams. An overview of the results of the atmospheric model intercomparison project (AMIP I). *Bull. Am. Meteorol. Soc.*, 80(1):29–55, January 1999. ISSN 0003-0007,1520-0477. doi: 10.1175/1520-0477(1999)080<0029:aootro>2.0.co;2.
- Krzysztof M Gorski, Eric Hivon, Anthony J Banday, Benjamin D Wandelt, Frode K Hansen, Mstvos Reinecke, and Matthias Bartelmann. Healpix: A framework for high-resolution discretization and fast analysis of data distributed on the sphere. *The Astrophysical Journal*, 622(2):759, 2005.

- Hans Hersbach, Bill Bell, Paul Berrisford, Shoji Hirahara, András Horányi, Joaquín Muñoz-Sabater, Julien Nicolas, Carole Peubey, Raluca Radu, Dinand Schepers, Adrian Simmons, Cornel Soci, Saleh Abdalla, Xavier Abellan, Gianpaolo Balsamo, Peter Bechtold, Gionata Biavati, Jean Bidlot, Massimo Bonavita, Giovanna Chiara, Per Dahlgren, Dick Dee, Michail Diamantakis, Rossana Dragani, Johannes Flemming, Richard Forbes, Manuel Fuentes, Alan Geer, Leo Haimberger, Sean Healy, Robin J Hogan, Elías Hólm, Marta Janisková, Sarah Keeley, Patrick Laloyaux, Philippe Lopez, Cristina Lupu, Gabor Radnoti, Patricia Rosnay, Iryna Rozum, Freja Vamborg, Sebastien Villaume, and Jean-Noël Thépaut. The ERA5 global reanalysis. *Quart. J. Roy. Meteor. Soc.*, 146(730):1999–2049, July 2020. ISSN 0035-9009,1477-870X. doi: 10.1002/qj.3803.
- Jonathan Ho, Ajay Jain, and Pieter Abbeel. Denoising diffusion probabilistic models. *arXiv [cs.LG]*, June 2020.
- Jonathan Ho, Chitwan Saharia, William Chan, David J Fleet, Mohammad Norouzi, and Tim Salimans. Cascaded diffusion models for high fidelity image generation. *J. Mach. Learn. Res.*, 23(47):47:1–47:33, May 2021. ISSN 1532-4435,1533-7928.
- Jonathan Ho, Tim Salimans, Alexey Gritsenko, William Chan, Mohammad Norouzi, and David J. Fleet. Video diffusion models, 2022. URL <https://arxiv.org/abs/2204.03458>.
- C. Hohenegger, P. Korn, L. Linardakis, R. Redler, R. Schnur, P. Adamidis, J. Bao, S. Bastin, M. Behraves, M. Bergemann, J. Biercamp, H. Bockelmann, R. Brokopf, N. Brüggemann, L. Casaroli, F. Chegini, G. Datsis, M. Esch, G. George, M. Giorgetta, O. Gutjahr, H. Haak, M. Hanke, T. Ilyina, T. Jahns, J. Jungclaus, M. Kern, D. Klocke, L. Kluft, T. Kölling, L. Kornbluh, S. Kosukhin, C. Kroll, J. Lee, T. Mauritsen, C. Mehlmann, T. Mieslinger, A. K. Naumann, L. Paccini, A. Peinado, D. S. Praturi, D. Putrasahan, S. Rast, T. Riddick, N. Roeber, H. Schmidt, U. Schulzweida, F. Schütte, H. Segura, R. Shevchenko, V. Singh, M. Specht, C. C. Stephan, J.-S. von Storch, R. Vogel, C. Wengel, M. Winkler, F. Ziemann, J. Marotzke, and B. Stevens. Icon-sapphire: simulating the components of the earth system and their interactions at kilometer and subkilometer scales. *Geoscientific Model Development*, 16(2):779–811, 2023. doi: 10.5194/gmd-16-779-2023. URL <https://gmd.copernicus.org/articles/16/779/2023/>.
- Matthias Karlbauer, Nathaniel Cresswell-Clay, Dale R Durran, Raul A Moreno, Thorsten Kurth, Boris Bonev, Noah Brenowitz, and Martin V Butz. Advancing parsimonious deep learning weather prediction using the HEALPix mesh. *J. Adv. Model. Earth Syst.*, 16(8), August 2024. ISSN 1942-2466. doi: 10.1029/2023ms004021.
- Tero Karras, Miika Aittala, Timo Aila, and Samuli Laine. Elucidating the design space of diffusion-based generative models, 2022.
- Diederik P Kingma and Jimmy Ba. Adam: A method for stochastic optimization. *arXiv [cs.LG]*, December 2014.
- Nikolay Koldunov, Tobias Kölling, Xabier Pedruzo-Bagazgoitia, Thomas Rackow, René Redler, Dmitry Sidorenko, Karl-Hermann Wieners, and Florian Andreas Ziemann. nextgems: output of the model development cycle 3 simulations for icon and ifs, 2023. URL https://doi.org/10.26050/WDCC/nextGEMS_cyc3.
- Nicoletta Krachmalnicoff and Maurizio Tomasi. Convolutional neural networks on the healpix sphere: a pixel-based algorithm and its application to cmb data analysis. *Astronomy & Astrophysics*, 628:A129, 2019.
- Remi Lam, Alvaro Sanchez-Gonzalez, Matthew Willson, Peter Wirnsberger, Meire Fortunato, Ferran Alet, Suman Ravuri, Timo Ewalds, Zach Eaton-Rosen, Weihua Hu, Alexander Merose, Stephan Hoyer, George Holland, Oriol Vinyals, Jacklynn Stott, Alexander Pritzel, Shakir Mohamed, and Peter Battaglia. Learning skillful medium-range global weather forecasting. *Science*, 382(6677):1416–1421, December 2023. ISSN 0036-8075,1095-9203. doi: 10.1126/science.adi2336.
- Christian Lessig, Iliana Luise, Bing Gong, Michael Langguth, Scarlet Stadtler, and Martin Schultz. AtmoRep: A stochastic model of atmosphere dynamics using large scale representation learning. *arXiv [physics.aoph]*, August 2023.

- Lizao Li, Robert Carver, Ignacio Lopez-Gomez, Fei Sha, and John Anderson. Generative emulation of weather forecast ensembles with diffusion models. *Sci Adv*, 10(13):eadk4489, March 2024. ISSN 2375-2548. doi: 10.1126/sciadv.adk4489.
- Xingchao Liu, Chengyue Gong, and Qiang Liu. Flow straight and fast: Learning to generate and transfer data with rectified flow. *arXiv [cs.LG]*, September 2022.
- Peter Manshausen, Yair Cohen, Jaideep Pathak, Mike Pritchard, Piyush Garg, Morteza Mardani, Karthik Kashinath, Simon Byrne, and Noah Brenowitz. Generative data assimilation of sparse weather station observations at kilometer scales. *arXiv [cs.LG]*, June 2024.
- Morteza Mardani, Noah Brenowitz, Yair Cohen, Jaideep Pathak, Chieh-Yu Chen, Cheng-Chin Liu, Arash Vahdat, Mohammad Amin Nabian, Tao Ge, Akshay Subramaniam, et al. Residual corrective diffusion modeling for km-scale atmospheric downscaling. *Communications Earth & Environment*, 6(1):124, 2025.
- Clifford Mass, David Ovens, John Christy, and Robert Conrick. The pacific northwest heat wave of 25–30 june 2021: Synoptic/mesoscale conditions and climate perspective. *Weather Forecast.*, 39(2):275–291, February 2024. ISSN 1520-0434,0882-8156. doi: 10.1175/waf-d-23-0154.1.
- Jaideep Pathak, Shashank Subramanian, Peter Harrington, Sanjeev Raja, Ashesh Chattopadhyay, Morteza Mardani, Thorsten Kurth, David Hall, Zongyi Li, Kamyar Azizzadenesheli, Pedram Hassanzadeh, Karthik Kashinath, and Animashree Anandkumar. FourCastNet: A global data-driven high-resolution weather model using adaptive fourier neural operators. *arXiv [physics.ao-ph]*, February 2022.
- Nathanaël Perraudin, Michaël Defferrard, Tomasz Kacprzak, and Raphael Sgier. Deepsphere: Efficient spherical convolutional neural network with healpix sampling for cosmological applications. *Astronomy and Computing*, 27:130–146, 2019.
- Ilan Price, Alvaro Sanchez-Gonzalez, Ferran Alet, Tom R Andersson, Andrew El-Kadi, Dominic Masters, Timo Ewalds, Jacklynn Stott, Shakir Mohamed, Peter Battaglia, Remi Lam, and Matthew Willson. Probabilistic weather forecasting with machine learning. *Nature*, pages 1–7, December 2024. ISSN 1476-4687,1476-4687. doi: 10.1038/s41586-024-08252-9.
- Yann Quilcaille, Lukas Gudmundsson, Lea Beusch, Mathias Hauser, and Sonia I Seneviratne. Showcasing mesmer-x: Spatially resolved emulation of annual maximum temperatures of earth system models. *Geophysical Research Letters*, 49(17):e2022GL099012, 2022.
- V. Brahmananda Rao, A. M. C. do Carmo, and Sergio H. Franchito. Seasonal variations in the southern hemisphere storm tracks and associated wave propagation. *Journal of the Atmospheric Sciences*, 59(6): 1029 – 1040, 2002. doi: 10.1175/1520-0469(2002)059<1029:SVITSH>2.0.CO;2. URL https://journals.ametsoc.org/view/journals/atsc/59/6/1520-0469_2002_059_1029_svitsh_2.0.co_2.xml.
- François Rozet and Gilles Louppe. Score-based data assimilation. In A. Oh, T. Naumann, A. Globerson, K. Saenko, M. Hardt, and S. Levine, editors, *Advances in Neural Information Processing Systems*, volume 36, pages 40521–40541. Curran Associates, Inc., 2023. URL https://proceedings.neurips.cc/paper_files/paper/2023/file/7f7fa581cc8a1970a4332920cdf87395-Paper-Conference.pdf.
- Uwe Schulzweida. Cdo user guide, October 2023. URL <https://doi.org/10.5281/zenodo.10020800>.
- S.I. Seneviratne, X. Zhang, M. Adnan, W. Badi, C. Derezynski, A. Di Luca, S. Ghosh, I. Iskandar, J. Kossin, S. Lewis, F. Otto, I. Pinto, M. Satoh, S.M. Vicente-Serrano, M. Wehner, and B. Zhou. *Weather and Climate Extreme Events in a Changing Climate*, page 1513–1766. Cambridge University Press, Cambridge, United Kingdom and New York, NY, USA, 2021. doi: 10.1017/9781009157896.013.
- Adam H Sobel, Johan Nilsson, and Lorenzo M Polvani. The weak temperature gradient approximation and balanced tropical moisture waves. *Journal of the atmospheric sciences*, 58(23):3650–3665, 2001.
- Yang Song, Jascha Sohl-Dickstein, Diederik P Kingma, Abhishek Kumar, Stefano Ermon, and Ben Poole. Score-based generative modeling through stochastic differential equations. *arXiv [cs.LG]*, November 2020a.

- Yang Song, Jascha Sohl-Dickstein, Diederik P Kingma, Abhishek Kumar, Stefano Ermon, and Ben Poole. Score-based generative modeling through stochastic differential equations. *arXiv [cs.LG]*, November 2020b.
- Yang Song, Jascha Sohl-Dickstein, Diederik P. Kingma, Abhishek Kumar, Stefano Ermon, and Ben Poole. Score-based generative modeling through stochastic differential equations, 2021. URL <https://arxiv.org/abs/2011.13456>.
- B. Stevens, S. Adami, T. Ali, H. Anzt, Z. Aslan, S. Attinger, J. Bäck, J. Baehr, P. Bauer, N. Bernier, B. Bishop, H. Bockelmann, S. Bony, G. Brasseur, D. N. Bresch, S. Breyer, G. Brunet, P. L. Buttigieg, J. Cao, C. Castet, Y. Cheng, A. Dey Choudhury, D. Coen, S. Crewell, A. Dabholkar, Q. Dai, F. Doblas-Reyes, D. Durran, A. El Gaidi, C. Ewen, E. Exarchou, V. Eyring, F. Falkinoff, D. Farrell, P. M. Forster, A. Frassoni, C. Frauen, O. Fuhrer, S. Gani, E. Gerber, D. Goldfarb, J. Grieger, N. Gruber, W. Hazeleger, R. Herken, C. Hewitt, T. Hoefler, H.-H. Hsu, D. Jacob, A. Jahn, C. Jakob, T. Jung, C. Kadow, I.-S. Kang, S. Kang, K. Kashinath, K. Kleinen-von Königsłow, D. Klocke, U. Kloenne, M. Klöwer, C. Kodama, S. Kollet, T. Kölling, J. Kontkanen, S. Kopp, M. Koran, M. Kulmala, H. Lappalainen, F. Latifi, B. Lawrence, J. Y. Lee, Q. Lejeun, C. Lessig, C. Li, T. Lippert, J. Luterbacher, P. Manninen, J. Marotzke, S. Matsouoka, C. Merchant, P. Messmer, G. Michel, K. Michielsen, T. Miyakawa, J. Müller, R. Munir, S. Narayanasetti, O. Ndiaye, C. Nobre, A. Oberg, R. Oki, T. Özkan-Haller, T. Palmer, S. Posey, A. Prein, O. Primus, M. Pritchard, J. Pullen, D. Putrasahan, J. Quaas, K. Raghavan, V. Ramaswamy, M. Rapp, F. Rauser, M. Reichstein, A. Revi, S. Saluja, M. Satoh, V. Schemann, S. Schemm, C. Schnadt Poberaj, T. Schulthess, C. Senior, J. Shukla, M. Singh, J. Slingo, A. Sobel, S. Solman, J. Spitzer, P. Stier, T. Stocker, S. Strock, H. Su, P. Taalas, J. Taylor, S. Tegtmeier, G. Teutsch, A. Tompkins, U. Ulbrich, P.-L. Vidale, C.-M. Wu, H. Xu, N. Zaki, L. Zanna, T. Zhou, and F. Ziemer. Earth virtualization engines (eve). *Earth System Science Data*, 16(4):2113–2122, 2024. doi: 10.5194/essd-16-2113-2024. URL <https://essd.copernicus.org/articles/16/2113/2024/>.
- Paul A. Ullrich, Colin M. Zarzycki, Elizabeth E. McClenny, Marielle C. Pinheiro, Alyssa M. Stansfield, and Kevin A. Reed. Tempestextremes v2.1: a community framework for feature detection, tracking, and analysis in large datasets. *Geoscientific Model Development (Online)*, 14(8), 8 2021. doi: 10.5194/gmd-14-5023-2021.
- Vikram Voleti, Alexia Jolicoeur-Martineau, and Christopher Pal. Mcvd: Masked conditional video diffusion for prediction, generation, and interpolation, 2022. URL <https://arxiv.org/abs/2205.09853>.
- Mengze Wang, Andre Nogueira Souza, Raffaele Ferrari, and Themistoklis Sapsis. Stochastic emulators of spatially resolved extreme temperatures of earth system models. *Authorea Preprints*, 2025. doi: 10.1029/2023ms004021.
- D Watson-Parris, Y Rao, D Olivie, Ø Seland, P Nowack, G Camps-Valls, P Stier, S Bouabid, M Dewey, E Fons, J Gonzalez, P Harder, K Jeggle, J Lenhardt, P Manshausen, M Novitasari, L Ricard, and C Roesch. ClimateBench v1.0: A benchmark for data-driven climate projections. *J. Adv. Model. Earth Syst.*, 14(10), October 2022. ISSN 1942-2466. doi: 10.1029/2021ms002954.
- Oliver Watt-Meyer, Brian Henn, Jeremy McGibbon, Spencer K Clark, Anna Kwa, W Andre Perkins, Elynn Wu, Lucas Harris, and Christopher S Bretherton. ACE2: Accurately learning subseasonal to decadal atmospheric variability and forced responses. *arXiv [physics.ao-ph]*, November 2024.

A Details for Z500-90p analysis

The methodology mirrors the tx90p analysis feature defined by Seneviratne et al. [2021] (See Fig. 11.9). First, percentiles of Z500 at 0 UTC are computed for each day of the year and spatial location using a 14-day rolling window. Specifically, we use the climate data operators [Schulzweida, 2023] `ydrunpct1` command with a 14-day window, and compute percentiles over 1990-2010.

Then, the fraction of samples exceeding this daily percentile climatology is computed for each year separately. The regression coefficients in Figure 10e,f are computed by fitting a regression line with least squares over the entire period we had ERA5 data for 1980-2018 (inclusive).

B Diurnal Cycle: Details

The diurnal amplitude is defined as

$$S := \frac{1}{366} \sum_d \max_h \bar{T}(d, h) - \min_h \bar{T}(d, h).$$

$\bar{T}(d, h)$ is the average of T as a function of day of year d and hour of day h . For the SNR computation, the noise is given by

$$N := \frac{1}{366} \sum_d \frac{1}{24} \sum_h s_T^2(d, h),$$

where s_T^2 is the conditional sample variance. In this computation, s_T^2 and \bar{T} are computed over 1990-2018 (inclusive). Then, the $SNR := S/N$.

C Architecture: Details

D Datasets: Details

E Pseudo-code for masking in the loss function

```
D_yn = net(where(mask, y + n, 0), sigma)
loss = weight * ((D_yn - where(mask, y, 0)) ** 2)
loss = where(mask, loss, 0) / mask.mean()
```

F Super-resolution results: Details

Super-resolution probability distribution Figure SI6 shows the probability distributions of surface air temperature and precipitation aggregating over all temporal and spatial locations. The super-resolution (red line) captures the shape of temperature and precipitation PDFs (Figure SI6a,c) including the correct power law regulating the heavy tail of low-likelihood extreme precipitation occurrence (Figure SI6c.).

Cascaded generations probability distribution Figure SI7 shows the probability distributions computed using 64 randomly selected samples spanning from March 6, 2024, to July 23, 2025. Overall, the distributions match well, though the cascaded model struggles to produce the coldest temperatures (less than -60 deg C). The super-resolution did not have this problem, which suggests that the bias likely comes from the coarse-resolution generations in this cascaded setup.

Multidiffusion Parameter Ablation The overlap size in multidiffusion sampling is a critical factor influencing both computational efficiency and output quality. Specifically, it determines the number of denoiser evaluations required: fewer evaluations reduce computational cost but can compromise visual consistency

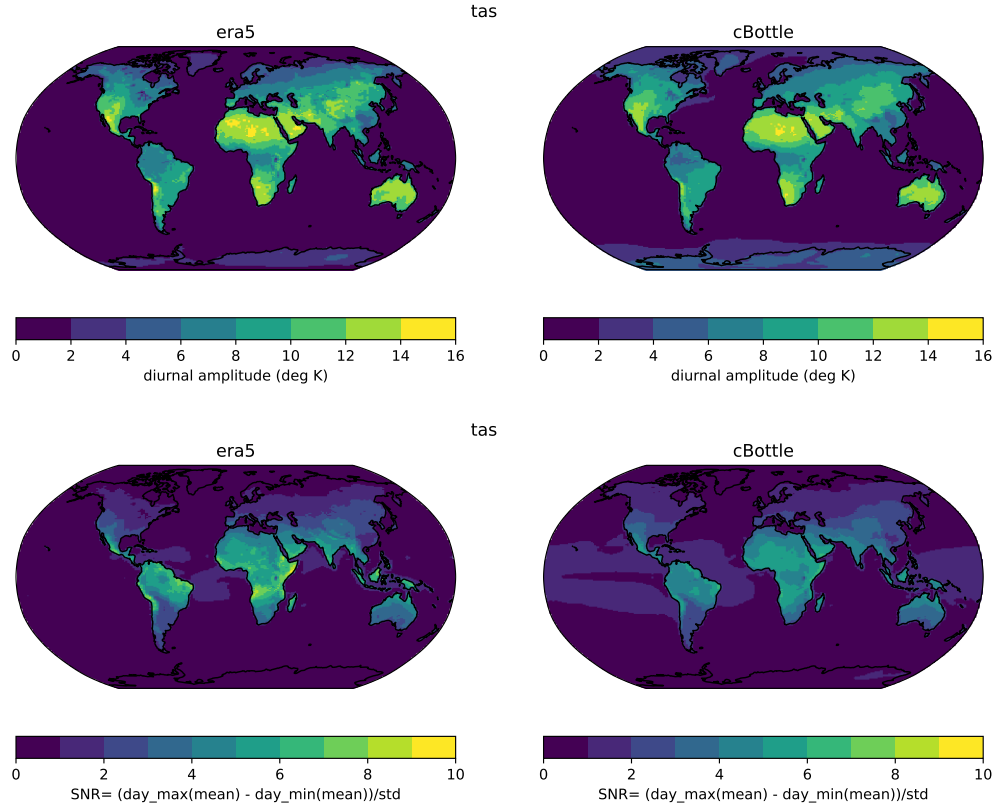


Figure SII: Diurnal cycle diagnostics for surface air temperature. (top row) Amplitude of the diurnal cycle. (bottom row) signal to noise ratio.

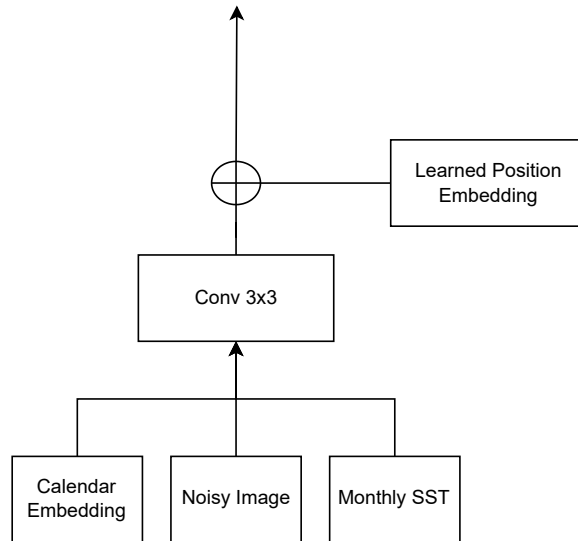


Figure SI2: Position and calendar embedding.

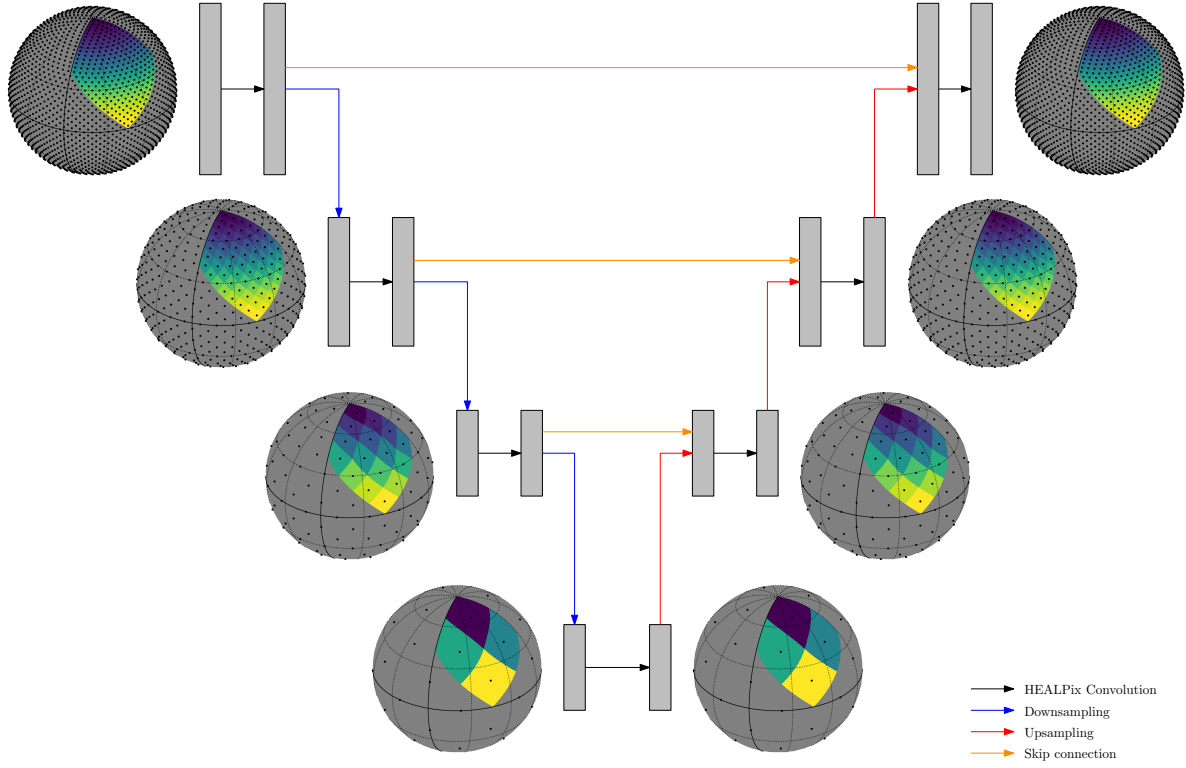


Figure SI3: Schematic showing the UNet architecture for spherical geometry with HEALPix grids. Each convolution is applied on HEALPix faces padded as in [Karlbauer et al., 2024].

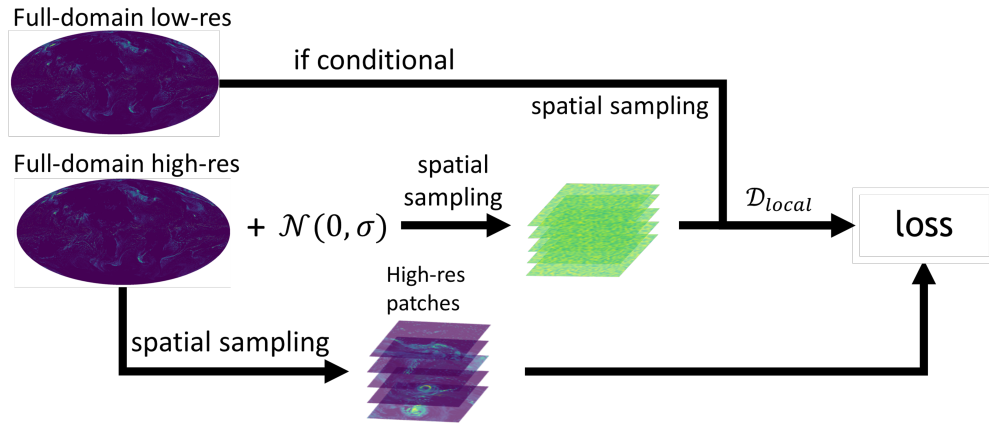


Figure SI4: Training workflow of the multi-diffusion framework. Global maps are decomposed into patches for parallel training of local denoisers conditioned on spatially aligned context.

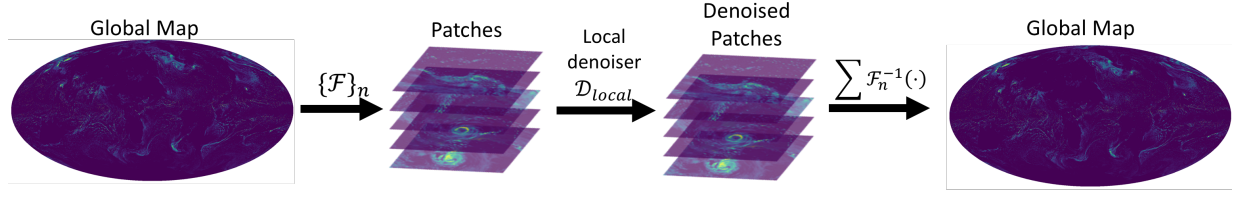


Figure SI5: Illustration of the aggregated local denoiser replacing the global denoiser in the sampling algorithm.

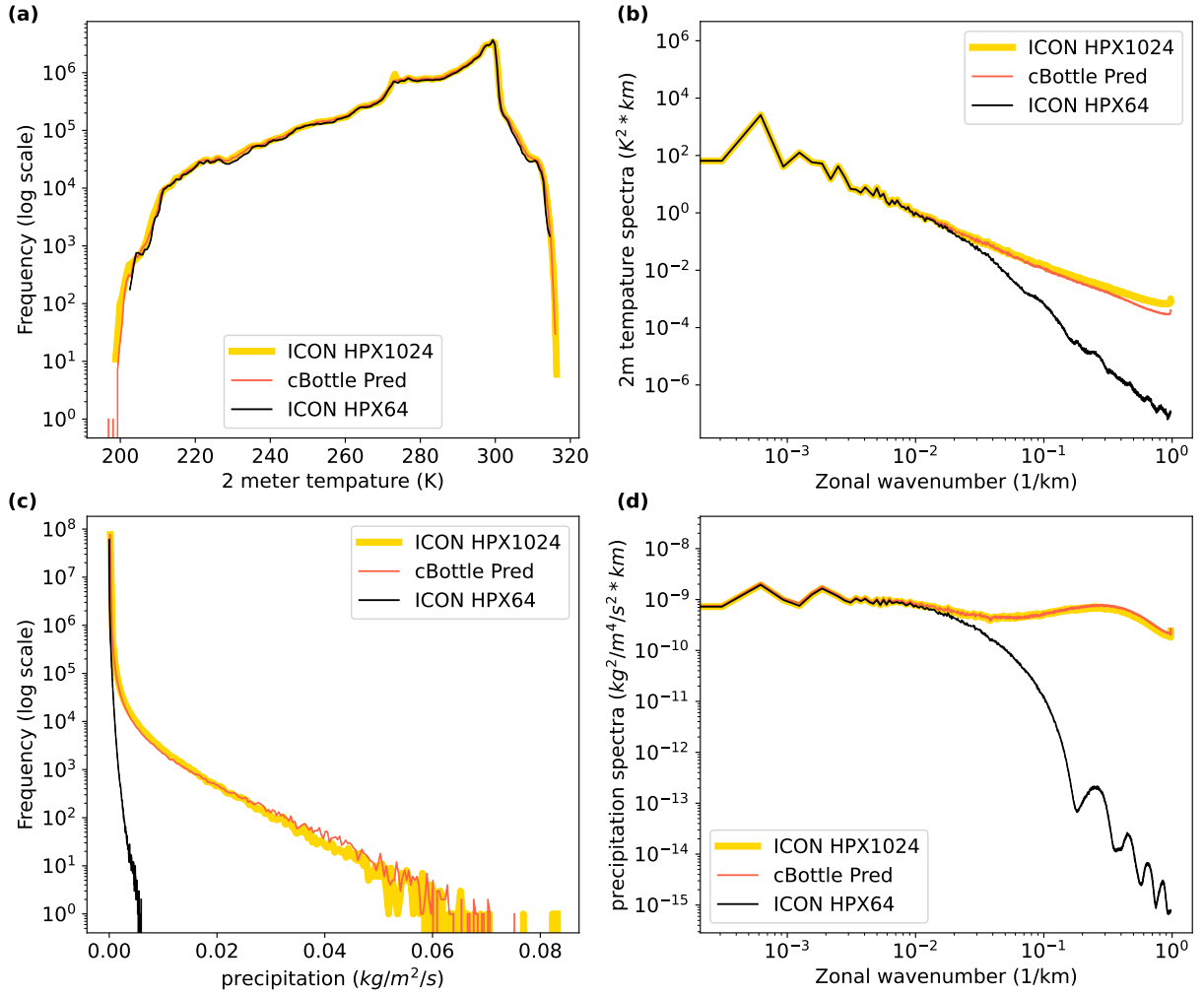


Figure SI6: Spherical power spectra and distribution plots of ICON HPX64 super-resolution inferences across 32 validation samples. (a), (c): power spectra for 2-meter temperature and precipitation. (b), (d): log-scale distributions of 2-meter temperature and precipitation.

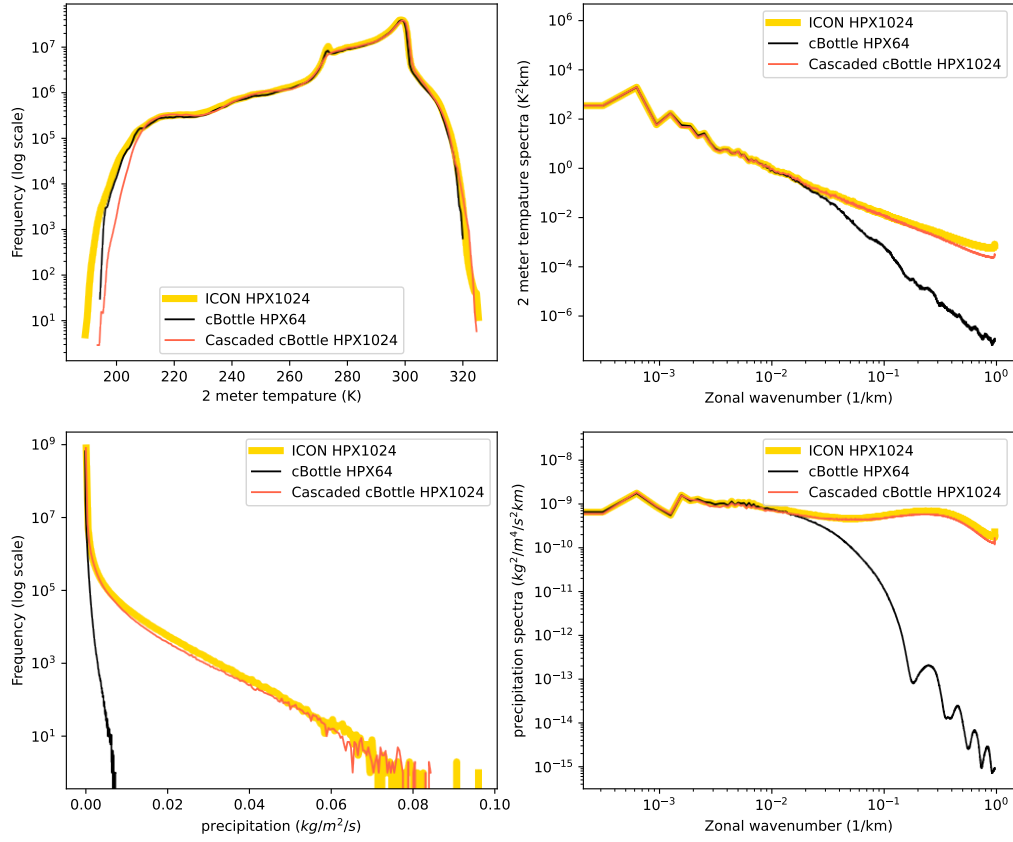


Figure SI7: Spherical power spectra and distribution plots of cascaded *cBottle* inferences across 64 validation samples. (a), (c): power spectra for 2-meter temperature and precipitation. (b), (d): log-scale distributions of 2-meter temperature and precipitation. Samples from cascaded and ICON are not matched.

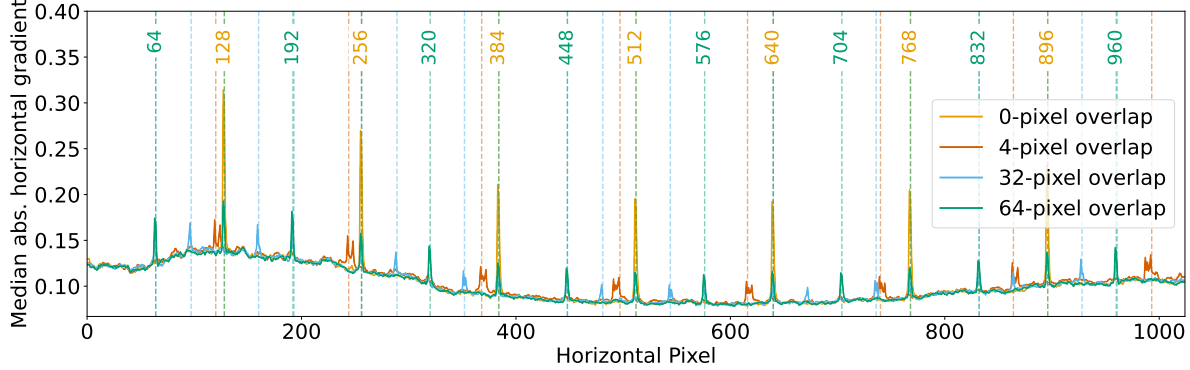


Figure SI8: Severity of patch artifacts across different overlapping pixel sizes, visualized using the mean absolute Sobel-X gradient of surface temperature field as a function of horizontal pixel position.

due to patch independence. A zero-overlap configuration, while minimizing runtime, often introduces visible artifacts at patch boundaries. Therefore, selecting an appropriate overlap size is essential to balancing reconstruction fidelity and efficiency.

To investigate this trade-off, we evaluate various overlap sizes using the median absolute horizontal Sobel gradient of surface temperature, as shown in Figure SI8. This metric serves as a proxy for boundary artifacts, where higher gradient magnitudes indicate sharper discontinuities. To generate the plot, we aggregate all faces from 16 randomly sampled outputs. A Sobel-X filter is applied to the surface temperature field, and the median of the resulting gradient magnitudes is computed across the face, sample, and vertical dimensions.

As expected, the 0-pixel overlap configuration exhibits pronounced, periodic spikes at 128-pixel intervals, indicating strong discontinuities at patch edges. The 64-pixel overlap shows secondary spikes at 64-pixel intervals. The 4-pixel overlap yields slightly stronger artifacts than the 32-pixel case, suggesting that very narrow overlaps may be insufficient to effectively smooth patch boundaries.

G Further climate diagnostics

G.1 Zonal Mean Precipitation

Figure SI11 examines mean precipitation in *cBottle* ERA5 and its relationship with latitude computed. Overall *cBottle* ERA5 captures the existence and correct positioning of local maxima associated with mid-latitude storm tracks and intertropical convergence zones straddling the equator. Local imperfections include positive biases in the northern (+4%) and southern (+11%) tropical rain bands, and as much as 11% underestimation of midlatitude rainfall. These differences can in part be explained partially by sampling error.

G.2 Power-spectral fidelity of the coarse-resolution generator

Figure SI12 shows that the spectra of the generated coarse samples are consistent with their ICON and ERA5 ground truth. For some fields, the ICON data shows significantly more power than ERA5 at large wave numbers, but we have not confirmed if this comes from the aliasing of smaller scale modes due to the block averaging used to coarsen the native HPX1024 outputs for ICON or an actual difference.

G.3 Submonthly variance

Figure SI14 maps summarize the pointwise variance of samples after removing the seasonal cycle, i.e. anomaly with respect to their monthly climatology (Figure SI14). This summarizes dispersion produced by a variety of sources including diurnal and synoptic variability. Variance of 500 hPa geopotential height (top) is maximized over the Southern Ocean, North Atlantic Sea and northeast Pacific due to midlatitude weather

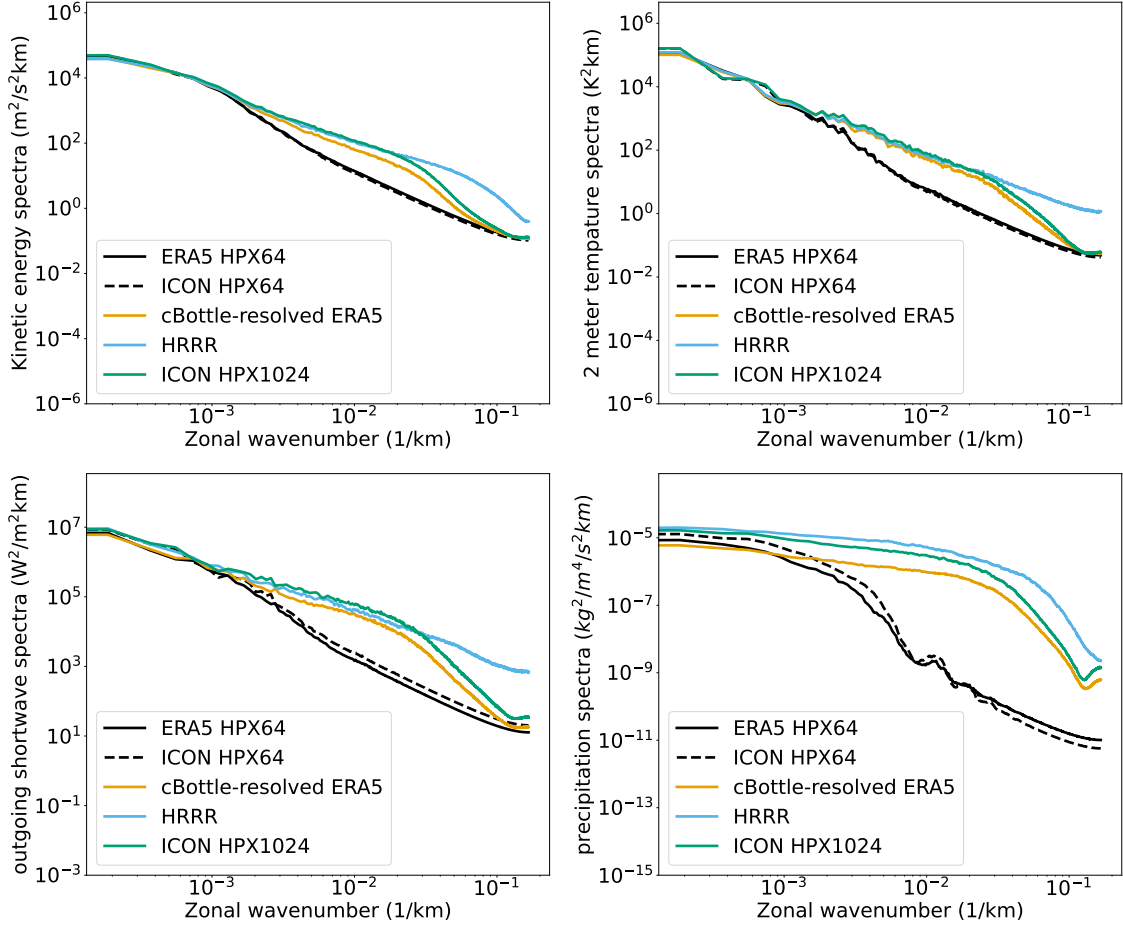


Figure SI9: Emulation of native-grid ICON with ERA5: Power spectra of cBottle-resolved ERA5 and various baselines, computed over 10 samples. All datasets are regridded to a Lambert-Conformal projection for comparison. ERA5, cBottle-resolved ERA5, and HRRR share an identical set of evaluation timestamps. ICON HPX64 and ICON HPX1024 use matching times of day and days of the year, but from different years.

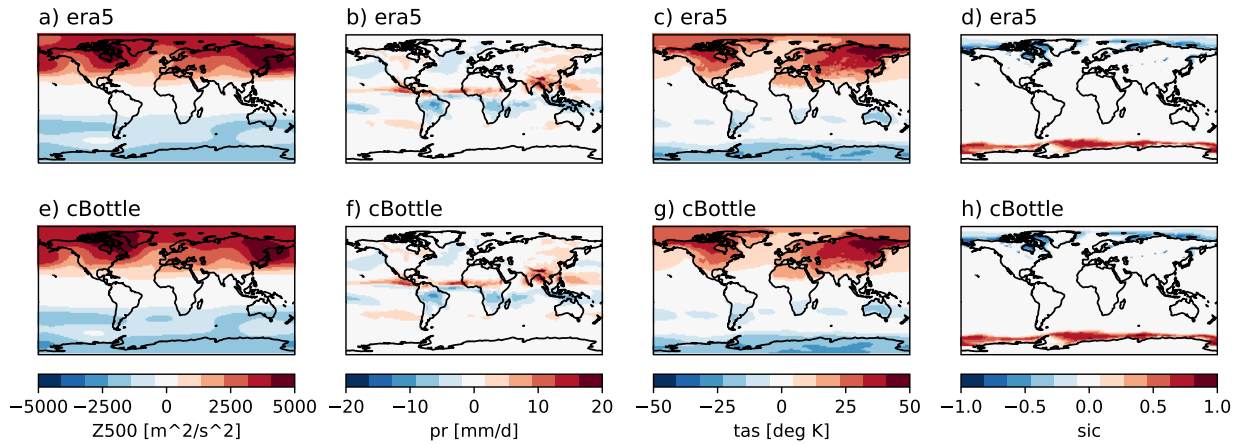


Figure SI10: Seasonal cycle for (JJA- DJF) for ERA5 and cBottle. Panels are shown for Z500, surface air temperature, precipitation, and sea ice concentration.

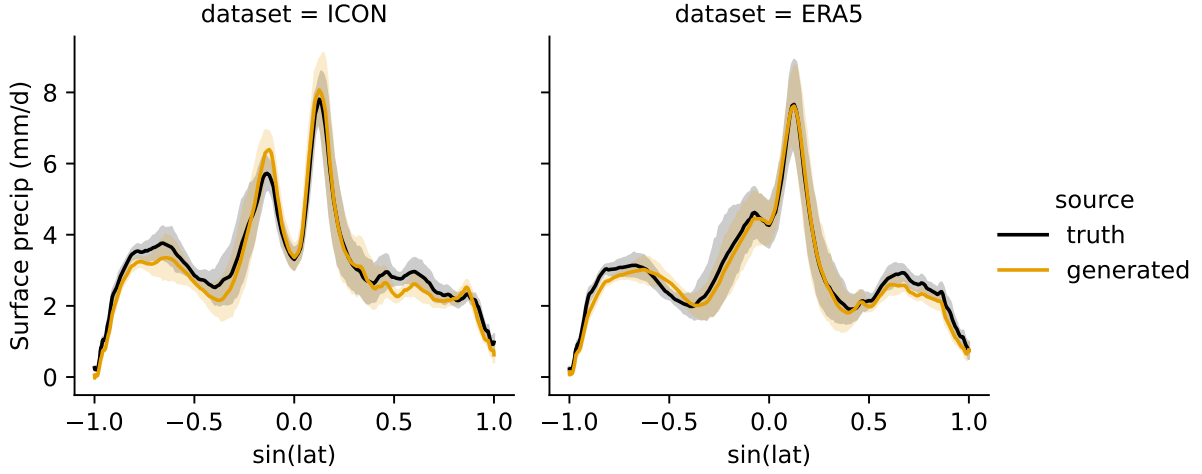


Figure SI11: Zonal Average of precipitation ICON, ERA5, and their emulators. 95% confidence intervals for the validation set means are estimated by bootstrapping over monthly averages. Only data from the validation periods for ICON and ERA5 are used.

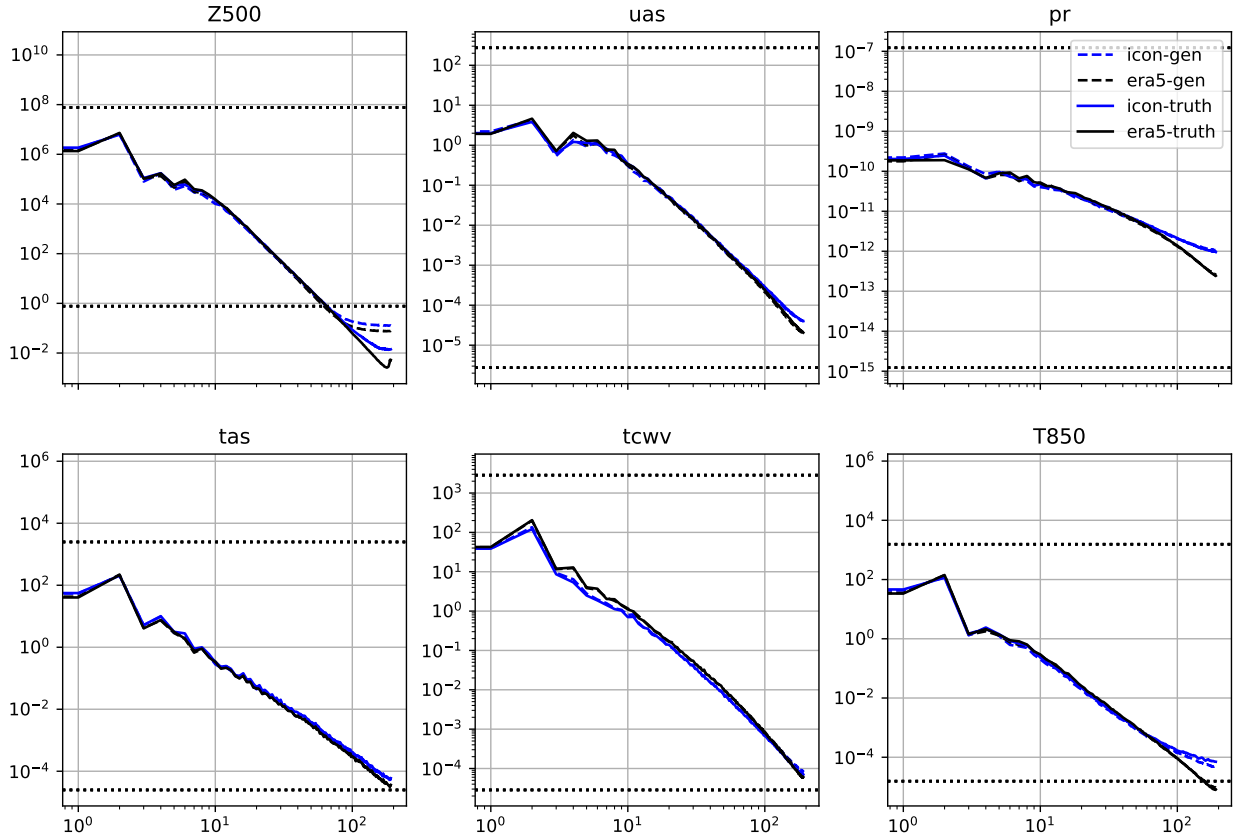


Figure SI12: (left) Spherical power spectra of versus the truth. Averages over 100 random samples from the test period are shown. The dotted lines indicate the range of noise levels used for the sampling $\sigma_{\{min,max\}}^2 \frac{4\pi}{n_{pix}}$. The factor of $\frac{4\pi}{n_{pix}}$ scales the pixel-wise variance to the same units as the power spectra, which is variance per surface area of the unit sphere.

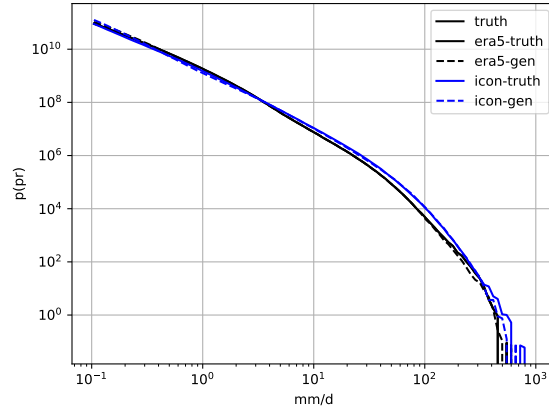


Figure SI13: PDF of instantaneous precipitation. Computed for same samples as in SI12.

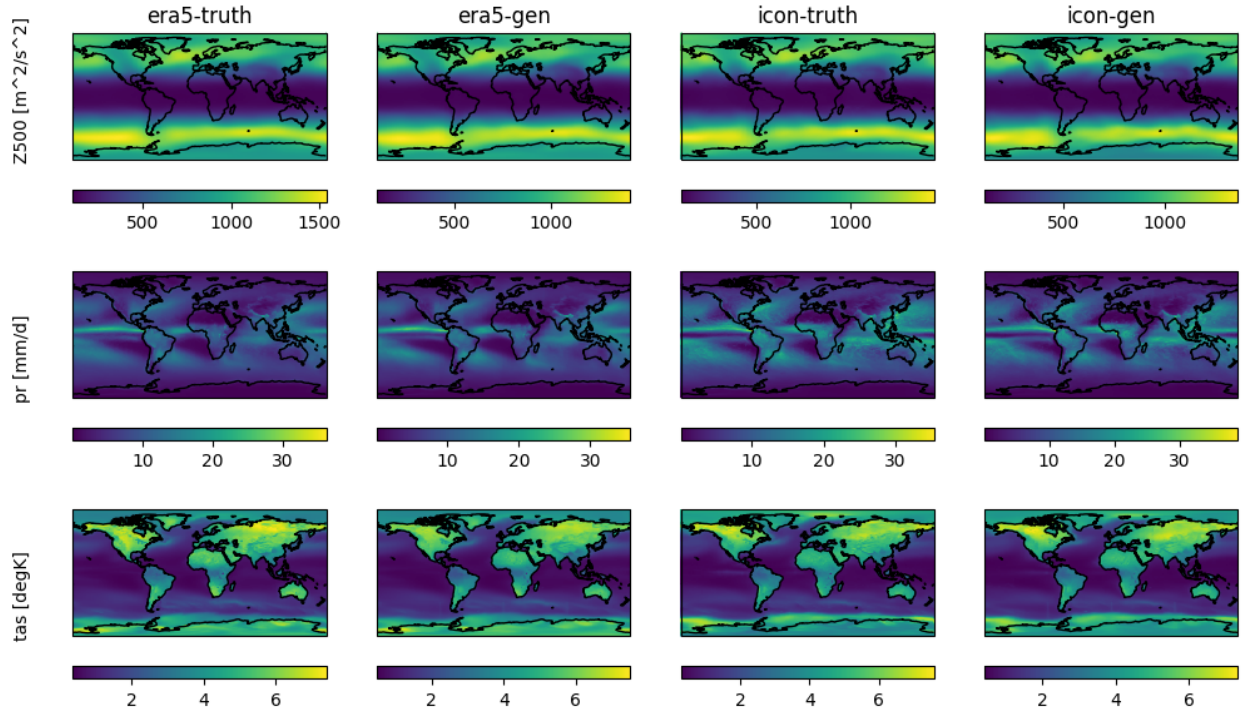


Figure SI14: Sub-monthly standard-deviation (variance from the monthly mean averaged over all months in the test period), surface air temperature, and precipitation. Panels are shown for the ground truth and *cBottle* for ICON and ERA5.

systems, but avoids the tropics due to the weak temperature gradient constraint there [Sobel et al., 2001]. Midlatitude rainfall variance occurs over the storm tracks including the Gulf Stream and Kuroshio currents. Rainfall variance is especially high within the intertropical convergence zones. In the special case of surface temperature, diurnal variability leads to a distinct land-sea contrast – a result of solar heating causing strong day-night temperature cycles over land, where surface specific heat capacity is relatively low.

The main point of Figure SI14 is that **cBottle-ERA5** and **cBottle-ICON** faithfully generate all of these pointwise variance features summarizing diurnal-to-synoptic variability – and with sufficient precision to detect differences between them, such as the “double ITCZ” – which manifests in **cBottle-ICON** and **cBottle-ICON-Target** as a zonal band of excessive dispersion in tropical rainfall in the eastern Pacific just south of the equator.

H Supplementary Figures

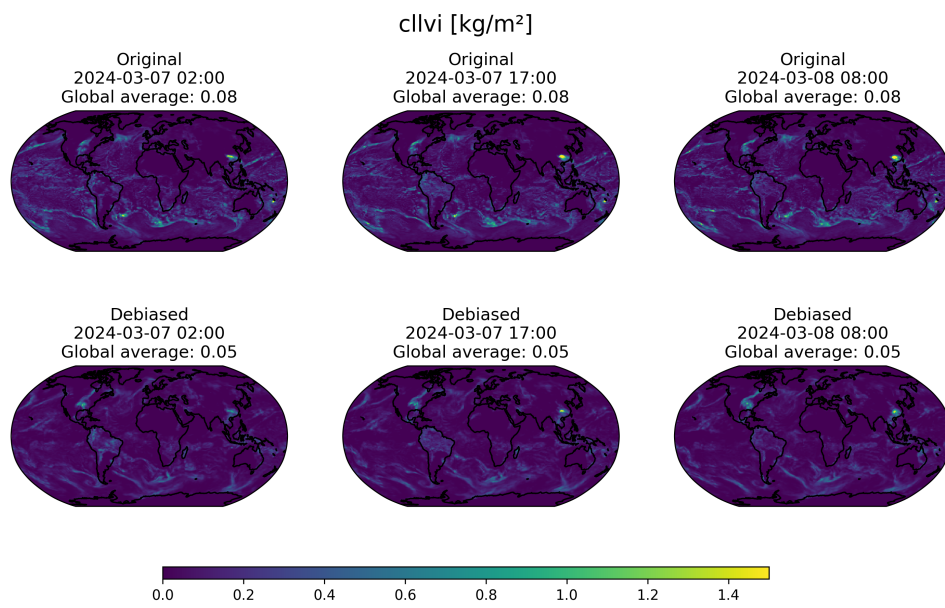


Figure SI15: Bias correction of the total cloud liquid water. (top) original ICON data and (bottom) bias corrected.